Effect of compressibility on the small-scale structures in isotropic turbulence

Jianchun Wang[1]†, **Yipeng Shi**[1], **Lian-Ping Wang**[2], **Zuoli Xiao**[1], **X. T. He**[1] **and Shiyi Chen**[1]†

[1]State Key Laboratory of Turbulence and Complex Systems, HEDPS and CAPT, College of Engineering, Peking University, Beijing 100871, P. R. China

[2]Department of Mechanical Engineering, University of Delaware, Newark, DE 19716, USA

Using a simulated highly compressible isotropic turbulence field with turbulent Mach number around 1.0, we studied the effects of local compressibility on the statistical properties and structures of velocity gradients in order to assess salient small-scale features pertaining to highly compressible turbulence against existing theories for incompressible turbulence. A variety of statistics and local flow structures conditioned on the local dilatation – a measure of local flow compressibility – are studied. The overall enstrophy production is found to be enhanced by compression motions and suppressed by expansion motions. It is further revealed that most of the enstrophy production is generated along the directions tangential to the local density isosurface in both compression and expansion regions. The dilatational contribution to enstrophy production is isotropic and dominant in highly compressible regions. The emphasis is then directed to the complicated properties of the enstrophy production by the deviatoric strain rate at various dilatation levels. In the overall flow field, the most probable eigenvalue ratio for the strain rate tensor is found to be $-3:1:2.5$, quantitatively different from the preferred eigenvalue ratio of $-4:1:3$ reported in incompressible turbulence. Furthermore, the strain rate eigenvalue ratio tends to be $-1:0:0$ in high compression regions, implying the dominance of sheet-like structures. The joint probability distribution function of the invariants for the deviatoric velocity gradient tensor is used to characterize local flow structures conditioned on the local dilatation as well as the distribution of enstrophy production within these flow structures. We demonstrate that strong local compression motions enhance the enstrophy production by vortex stretching, while strong local expansion motions suppress enstrophy production by vortex stretching. Despite these complications, most statistical properties associated with the solenoidal component of the velocity field are found to be very similar to those in incompressible turbulence, and are insensitive to the change of local dilatation. Therefore, a good understanding of dynamics of the compressive component of the velocity field is key to an overall accurate description of highly compressible turbulence.

Key words: compressible turbulence, isotropic turbulence, turbulence simulation

† Email addresses for correspondence: jwang.pku@gmail.com, syc@pku.edu.cn

1. Introduction

The small-scale dynamics in fluid turbulence is characterized by velocity gradients and is relevant to many important turbulent flow processes, including viscous dissipation of kinetic energy, intermittency, vortex self-stretching, and enstrophy production. There have been many studies on statistical properties of the velocity gradient tensor, vorticity, and strain rate tensor for incompressible turbulent flows: see e.g. Meneveau (2011) and references therein. Ashurst *et al.* (1987) pioneered the investigation of the orientation of vorticity with eigenvectors of the strain rate tensor in the numerical simulation of incompressible turbulence. They observed that the vorticity tends to be aligned with the intermediate strain rate eigenvector. They also reported that the eigenvalues of the strain rate tensor have a preferred ratio of −4:1:3 in the highly dissipative regions. Tsinober, Kit & Dracos (1992) reported experimental investigations of velocity gradients in both homogeneous and inhomogeneous incompressible turbulence. They confirmed this strong tendency for the vorticity to align with the intermediate strain rate eigenvector and the vortex stretching vector, and obtained a preferred eigenvalue ratio of −3.8:1.0:3.1. Later, these behaviours were observed in a wide variety of incompressible turbulence: see Galanti & Tsinober (2000), Kholmyansky, Tsinober & Yorish (2001), Lüthi, Tsinober & Kinzelbach (2005) and Meneveau (2011).

Compared to incompressible turbulence, the small-scale features of compressible turbulence are much less studied. The effects of randomly distributed spatially varying shocks and compressibility on the dynamics and structures of velocity gradients represent a complex nonlinear problem. There have been a limited studies of the vorticity field and the strain rate tensor in compressible turbulent flows. Erlebacher & Sarkar (1993) investigated the velocity derivatives in a weakly compressible homogeneous shear turbulence. They reported a preferred strain rate eigenvalue ratio of −4:1:3 and confirmed the similar alignment of vorticity and the strain rate eigenvectors as in the incompressible flow. Their results state that the statistics of velocity gradients are not significantly affected by compressibility when the turbulent Mach number is less than 0.3. To clearly separate out the compressible effect, they performed the Helmholtz decomposition on the strain rate tensor. They then found that the most probable eigenvalue ratio for the compressive strain rate tensor was −2.2:1:1.2 for high dilatation regions, indicating that sheet-like structures dominate in strong compression regions. Pirozzoli & Grasso (2004) carried out direct numerical simulations of decaying isotropic compressible turbulence at various initial turbulent Mach numbers (0.1–0.8). They found that the eigenvalues of the strain rate tensor have a preferred ratio of −4:1:3 in all their simulations. They also showed that the shape of the probability density function (p.d.f.) of the angle between vorticity and three strain rate eigenvectors is independent of the initial turbulent Mach number. Later, Lee, Girimaji & Kerimo (2009) performed numerical simulation of isotropic turbulence with an initial turbulent Mach number up to 0.885. They again found that the eigenvalue ratio of −4:1:3 is preferred at all turbulent Mach numbers that they considered, and the alignment of vorticity relative to strain rate eigenvectors is similar in compressible and incompressible turbulence. Furthermore, they studied the effect of dilatation level on the preferential alignment between vorticity and strain rate eigenvectors, and concluded that this alignment is weakened in the strong dilatation regions.

Investigations of the physical-space local flow structures of small-scale turbulence have been made over the years. Chong *et al.* (1990) proposed a topological approach to classification of elementary three-dimensional flow patterns based on the relations of

three invariants of the deformation rate tensor in the velocity field. In incompressible turbulence, the first invariant of the deformation rate tensor is null due to continuity. Thus the local flow topology can be fully characterized by the second and third invariants of the deformation rate tensor. A universal teardrop shape of the joint p.d.f. of the second and third invariants of the deformation tensor was observed for a wide variety of incompressible turbulence, including mixing layers (Soria *et al.* 1994), wall-bounded turbulence (Blackburn, Mansour & Cantwell 1996; Chong *et al.* 1998), isotropic turbulence (Ooi *et al.* 1999), and the turbulence/non-turbulence interface in the jets (da Silva & Pereira 2008).

Pirozzoli & Grasso (2004) studied the joint p.d.f. of the second and third invariants of the deviatoric deformation tensor in decaying compressible isotropic turbulence. They found that the joint p.d.f. at various initial turbulent Mach numbers shares the same teardrop shape found in incompressible turbulence. They also showed that the conditional average of the second invariant of the deviatoric deformation rate tensor always scales with the 1/3 power of the discriminant of that tensor in their simulations. In the work by Suman & Girimaji (2010), the effect of compressibility on the topological structures of turbulent flow was demonstrated by the joint p.d.f. of the normalized second and third invariants of the deformation rate tensor conditioned on the dilatation levels. They concluded that, at low dilatation levels, local flow topology is very similar to incompressible turbulence, while at high dilatation levels, the flow structures are changed dramatically.

In this paper, we use flow fields from a forced isotropic turbulence with turbulent Mach number around 1.0, simulated on a 1024^3 grid using a novel computational approach (Wang *et al.* 2010), to examine in detail the properties of velocity gradients and their topology in a highly compressible turbulent flow. A systematic investigation of the effects of local dilatation is undertaken by means of conditional averages and conditional probability distribution functions, which separates this study from most previous studies of compressible turbulence. Furthermore, we analyse the conditional statistics of solenoidal component and compressive component of the velocity gradients, in order to better understand and interpret the conditional statistics of the full velocity gradients and to facilitate comparison with existing knowledge of incompressible turbulence. A similar approach is used to explore the effect of compressibility on local flow topological structures and enstrophy production in these various flow structures. Throughout the paper, a specific focus is placed on the properties of enstrophy production. We hope that this in-depth comprehensive analysis will advance our understanding of small-scale features in highly compressible turbulence. The large amount of conditional statistics to be reported here will serve to guide the development of accurate models of compressible turbulence in the future.

This paper is part of a systematic study of highly compressible turbulence. In a companion paper (Wang *et al.* 2011), we have examined carefully the flow statistics and structures near shocklets to assess how shocklets modify the small-scale flow field. We have demonstrated that, even for a highly compressible turbulence, the properties and structures of the solenoidal component of the velocity gradient tensor are nearly independent of the shock discontinuities.

In another companion paper (Wang *et al.* 2012), we have focused on the scaling properties of velocity increments and the power-law tail of the p.d.f. of the velocity divergence in high compression regions. We found that the two-point statistics of the solenoidal component of velocity field are not significantly different from those of

incompressible turbulence, but the scaling exponents of the velocity structure function for the compressive component become saturated at ∼0.7 at higher orders. We also showed that the power-law exponent of the p.d.f. of the velocity divergence is different from that found for Burgers turbulence. Using an analytical model, we related this difference to a major contribution from the pressure effect which is absent in the Burgers turbulence.

This paper is organized as follows. The governing equations and key parameters, along with the computational approach, are described in § 2. The general statistics of the simulated flow are provided in § 3. The effects of local dilatation on vorticity, strain rate tensor, and enstrophy production are analysed in § 4 through conditional statistics, along with visualization of flow structures in compression and expansion regions. In § 5 we discuss local flow topology and enstrophy production in various flow structures as classified by deviatoric velocity gradient invariants. Finally, our main conclusions are summarized in § 6.

2. Governing equations, system parameters, and simulation method

We consider a stationary compressible turbulence of an ideal gas driven and maintained by large-scale momentum forcing and thermal forcing. Following Samtaney, Pullin & Kosovic (2001), we shall introduce a set of reference scales to normalize the hydrodynamic and thermodynamic variables. Since these variables together contain four elemental dimensions, we first introduce four elemental reference scales, namely, a reference length L, velocity U, density ρ_0, and temperature T_0. The energy content of an ideal gas is fully specified by two specific heats: the specific heat at constant pressure C_p and the specific heat at constant volume C_v. These introduce a fluid property, namely, the specific heat ratio $\gamma \equiv C_p/C_v$, which is assumed to be equal to 1.4 in this study. The specific gas constant R is related to the specific heats by $R = C_p - C_v$. The derived reference scales are a reference speed of sound $c_0 \equiv \sqrt{\gamma R T_0}$, energy per unit volume $\rho_0 U^2$, and pressure $\rho_0 R T_0$. We then introduce the first reference governing parameter, the reference Mach number $M = U/c_0$. We further add a reference viscosity μ_0 and thermal conductivity κ_0, which introduce two additional governing parameters of the system: the reference Prandtl number $Pr \equiv \mu_0 C_p/\kappa_0$ and the reference Reynolds number $Re \equiv \rho_0 UL/\mu_0$. In this study, Pr is set to 0.7. Therefore, the flow system has two governing parameters: M and Re.

In terms of these normalization scales, the governing equations of the compressible flow system, in dimensionless form, are written as

$$\frac{\partial \rho}{\partial t} + \frac{\partial (\rho u_j)}{\partial x_j} = 0, \tag{2.1}$$

$$\frac{\partial (\rho u_i)}{\partial t} + \frac{\partial \left[\rho u_i u_j + p\delta_{ij}/\gamma M^2 \right]}{\partial x_j} = \frac{1}{Re} \frac{\partial \sigma_{ij}}{\partial x_j} + \mathscr{F}_i, \tag{2.2}$$

$$\frac{\partial \mathscr{E}}{\partial t} + \frac{\partial \left[(\mathscr{E} + p/\gamma M^2) u_j \right]}{\partial x_j} = \frac{1}{\alpha} \frac{\partial}{\partial x_j} \left(\kappa \frac{\partial T}{\partial x_j} \right) + \frac{1}{Re} \frac{\partial (\sigma_{ij} u_i)}{\partial x_j} - \Lambda + \mathscr{F}_j u_j, \tag{2.3}$$

$$p = \rho T, \tag{2.4}$$

where $\alpha \equiv Pr\, Re(\gamma - 1)M^2$. The primary variables of the system are the velocity vector u_i, density ρ, temperature T, and pressure p. The viscous stress σ_{ij}, and total energy

(internal plus kinetic energy) per unit volume $\mathscr{E}$ are defined by

$$\sigma_{ij} \equiv \mu \left(\frac{\partial u_i}{\partial x_j} + \frac{\partial u_j}{\partial x_i} \right) - \frac{2}{3} \mu \theta \delta_{ij}, \tag{2.5}$$

$$\mathscr{E} \equiv \frac{p}{(\gamma - 1)\gamma M^2} + \frac{1}{2}\rho(u_j u_j), \tag{2.6}$$

where $\theta \equiv \partial u_k / \partial x_k$ is the normalized velocity divergence or dilatation, a flow variable that measures the local rate of expansion (if $\theta > 0$) or compression (if $\theta < 0$).

The compressible flow system is completed by specifying a temperature-dependent dimensionless viscosity μ and thermal conductivity κ, as well as forcing methods used for $\mathscr{F}_i$ and Λ. These details are described in Wang *et al.* (2010). The system is solved numerically by using a hybrid approach in a cubic box with periodic boundary conditions. The hybrid scheme utilizes a seventh-order weighted essentially non-oscillatory (WENO) scheme (Balsara & Shu 2000) for shocklet regions and an eighth-order compact central finite difference scheme (Lele 1992) for smooth regions outside shocklets. Further details of the computational approach have been described in Wang *et al.* (2010).

In order to assess any dependence of small-scale statistics of the flow field on the grid resolution, three grid resolutions (512^3, 768^3 and 1024^3) were considered in this paper. After the system reached the statistically stationary state, a total of 20 flow fields spanning the time period of $2.68 \leqslant t/T_e \leqslant 4.63$ were used to obtain statistical averages of interested quantities, where T_e is the large eddy turnover time. The simulated compressible turbulence is governed by two important parameters, namely, the Taylor microscale Reynolds number Re_λ and the turbulent Mach number M_t (Samtaney *et al.* 2001). They are related to the two reference governing parameters Re and M by

$$Re_\lambda = Re \frac{u' \lambda \langle \rho \rangle}{\sqrt{3} \langle \mu \rangle}, \quad M_t = M \frac{u'}{\langle \sqrt{T} \rangle}, \tag{2.7}$$

where the r.m.s. fluctuation velocity magnitude is computed by $u' \equiv \sqrt{\langle u_1^2 + u_2^2 + u_3^2 \rangle}$, and the normalized Taylor microscale λ is defined by

$$\lambda = \sqrt{\frac{u'^2}{\langle (\partial u_1/\partial x_1)^2 + (\partial u_2/\partial x_2)^2 + (\partial u_3/\partial x_3)^2 \rangle}}. \tag{2.8}$$

By setting $Re = 1000$ and $M = 0.45$, we obtained an average turbulent Mach number around $M_t = 1.0$ and Taylor microscale Reynolds number around $Re_\lambda = 250$ for all simulations.

3. General statistics of the simulated flow

Table 1 summarizes some overall statistics of the flow fields for all simulations. The resolution parameters $k_{max}\eta$ are, respectively, 1.65, 2.47 and 3.33, where the Kolmogorov length scales $\eta = [\langle \mu / (Re\rho) \rangle^3 / \langle \epsilon/\rho \rangle]^{1/4}$ are all around 0.0065 and the largest wavenumbers k_{max} are, respectively, 256, 384 and 512. The statistics shown in table 1 imply that the small-scale flow is well resolved in the 1024^3 simulation. The integral length scale L_f is computed by

$$L_f = \frac{3\pi}{2(u')^2} \int_0^\infty \frac{E(k)}{k} \, dk, \tag{3.1}$$

Resolution	Re_λ	M_t	$k_{max}\eta$	u'	L_f	L_f/η	$\langle\epsilon\rangle$	θ'	ω'	S_3
512^3	256	1.02	1.65	2.15	1.45	224	0.529	7.3	22.9	−1.4
768^3	258	1.00	2.47	2.13	1.46	226	0.533	7.7	22.5	−1.9
1024^3	254	1.03	3.33	2.16	1.46	225	0.535	7.9	22.8	−2.2

TABLE 1. Simulation parameters and resulting flow statistics.

M^{rms}	$(u^s)'$	$(u^c)'$	$u^{c'}/u^{s'}$	θ'/ω'	$\rho'/\overline{\rho}$	$\langle\epsilon_s\rangle/\langle\epsilon\rangle$	$\langle\epsilon_c\rangle/\langle\epsilon\rangle$	E_k	E_I	$\langle p\theta/(\gamma M^2)\rangle$
1.01	2.11	0.46	0.22	0.35	0.28	88.2 %	13.8 %	2.11	8.12	−0.0175

TABLE 2. Parameters and resulting flow statistics for 1024^3 simulation.

where $E(k)$ is the spectrum of kinetic energy per unit mass, namely, $\int_0^\infty E(k)\,\mathrm{d}k = (u')^2/2$. The ratio L_f/η represents the range of scales in the simulated flow. The average dissipation rate $\langle\epsilon\rangle \equiv \langle\sigma_{ij}S_{ij}/Re\rangle$ represents the rate of conversion of kinetic energy to internal energy by viscous effects. The r.m.s. vorticity magnitude is computed by $\omega' = \sqrt{\langle\omega_1^2 + \omega_2^2 + \omega_3^2\rangle}$. The r.m.s. dilatation is found to be $\theta'/\omega' = 0.34$, indicating that the compressibility effect makes a significant contribution to velocity gradient statistics. This is further demonstrated by the magnitude of the velocity derivative skewness which is defined by

$$S_3 = \frac{\left[\left\langle(\partial u_1/\partial x_1)^3 + (\partial u_2/\partial x_2)^3 + (\partial u_3/\partial x_3)^3\right\rangle\right]/3}{\left\{\left\langle(\partial u_1/\partial x_1)^2 + (\partial u_2/\partial x_2)^2 + (\partial u_3/\partial x_3)^2\right\rangle/3\right\}^{3/2}}. \qquad (3.2)$$

Values of $S_3 = -1.4$, $S_3 = -1.9$ and $S_3 = -2.2$ are obtained in our three simulations; these are much larger than typical values of -0.4 to -0.6 found in the incompressible turbulence (Ishihara *et al.* 2007). The deviation is caused by the frequent formation of shocklets in the compressible turbulence.

In summary, the overall statistics of the flow field at the 1024^3 grid resolution are all well converged. Further details will be shown later in the paper. Unless indicated otherwise, the results shown in the rest of the paper are based on the 1024^3 flow simulation.

To help clarify the underlying physics in the compressible turbulence and specifically the effects of local compressibility, we shall employ the well-known Helmholtz decomposition (Erlebacher & Sarkar 1993; Samtaney *et al.* 2001) to the velocity field

$$\boldsymbol{u} = \boldsymbol{u}^s + \boldsymbol{u}^c, \qquad (3.3)$$

where the solenoidal component $\boldsymbol{u}^s$ satisfies $\nabla\cdot\boldsymbol{u}^s = 0$, and the compressive component $\boldsymbol{u}^c$ is irrotational, i.e. $\nabla\times\boldsymbol{u}^c = 0$.

In table 2, we compile relevant statistics related to the flow compressibility and the Helmholtz decomposition. The r.m.s. Mach number, $M^{rms} = \sqrt{\langle M_{loc}^2\rangle}$, was found to be 1.01, which is very close to the turbulent Mach number, where $M_{loc} = M\sqrt{u_1^2 + u_2^2 + u_3^2}/\sqrt{T}$ is the local Mach number. The ratio of the r.m.s. fluctuations of the two velocity components, $u^{c'}/u^{s'}$, is equal to 0.22, implying that the

compressible component contributes to a small but finite fraction of the total kinetic energy. The ratio 0.22 is comparable to 0.18 reported in Porter, Pouquet & Woodward (2002) for a very similar turbulent Mach number (0.97) in driven supersonic flows. The ratio θ'/ω' is equal to 0.35, significantly larger than $u^{c\prime}/u^{s\prime}$. This implies that the compressive effect plays a more significant role at small scales. The normalized density fluctuation $\rho'/\bar{\rho}$ was 0.28, where $\rho' \equiv \sqrt{\langle \rho^2 - \langle \rho \rangle^2 \rangle}$.

The kinetic energy is governed by the following equation (Andreopoulos, Agui & Briassulis 2000):

$$\rho \frac{\mathrm{D}}{\mathrm{D}t}\left(\frac{1}{2}u_i u_i\right) = \frac{\partial}{\partial x_j}\left(-\frac{1}{\gamma M^2}p u_j + \sigma_{ij}u_i\right) + \frac{1}{\gamma M^2}p\theta - \frac{\mu}{Re}\omega_i\omega_i$$
$$- \frac{4}{3}\frac{\mu}{Re}\theta^2 - 2\frac{\mu}{Re}\left(\frac{\partial u_i}{\partial x_j}\frac{\partial u_j}{\partial x_i} - \theta^2\right) + \mathscr{F}_j u_j. \tag{3.4}$$

Taking the volume average and observing periodic boundary conditions, we obtain

$$\frac{\mathrm{d}}{\mathrm{d}t}\left\langle \frac{1}{2}\rho u_i u_i \right\rangle = \frac{1}{\gamma M^2}\langle p\theta \rangle - \frac{1}{Re}\langle \mu\omega^2 \rangle - \frac{4}{3Re}\langle \mu\theta^2 \rangle$$
$$- \frac{2}{Re}\left\langle \mu\left(\frac{\partial u_i}{\partial x_j}\frac{\partial u_j}{\partial x_i} - \theta^2\right)\right\rangle + \langle \mathscr{F}_j u_j \rangle. \tag{3.5}$$

The first term on the right-hand side is the average pressure work, and we found that $\langle (1/\gamma M^2)p\theta \rangle = -0.0175$. The local pressure work $p\theta/(\gamma M^2)$ is positive in the expansion region and negative in the compression region; when combined, however, the net contribution to the kinetic energy appears to be small. This indicates that the pressure work locally causes energy exchanges between kinetic energy and internal energy, but the total energy transfer by the pressure work in the whole field is insignificant.

The net viscous dissipation rate is much larger, with $\langle \epsilon \rangle = \langle \sigma_{ij}S_{ij}/Re \rangle = 0.535$. This net dissipation is decomposed into three components, the solenoidal dissipation $\epsilon_s = (\mu/Re)\omega_i\omega_i$, the dilatational dissipation $\epsilon_c = (4/3)(\mu/Re)\theta^2$, and the mixed term $\epsilon_m = (2\mu/Re)((\partial u_i/\partial x_j)(\partial u_j/\partial x_i) - \theta^2)$, which represents the contributions to the dissipation rate by the purely non-homogeneous part of the flow (Andreopoulos *et al.* 2000). The mixed term is zero for an incompressible turbulence with constant viscosity. We found that $\langle \epsilon_c \rangle/\langle \epsilon_s \rangle = 0.157$ and $\langle \epsilon_m \rangle/\langle \epsilon_s \rangle = -0.023$. The ratio of kinetic energy to internal energy per unit volume is about $E_k/E_I = 0.260$, where $E_k = \langle \rho u_j u_j \rangle/2$ and $E_I = \langle p \rangle/[(\gamma - 1)\gamma M^2]$. This ratio depends on the turbulent Mach number. An estimation by $E_k/E_I \approx (\gamma - 1)\gamma M_t^2/2$ would give a value of 0.30. These data suggest that the contributions due to the compressibility effect are significant. The forcing term has an average value $\langle \mathscr{F}_j u_j \rangle = 0.52$, so the main balance is between the forcing and the viscous dissipation.

Figure 1 shows compensated power spectra of the velocity field $\boldsymbol{u}$ from all resolutions. The power spectra from the 768^3 resolution and the 1024^3 resolution overlap in almost all scale ranges, implying the convergence of the velocity power spectra under this grid refinement. Further, there is a narrow inertial subrange with a Kolmogorov constant around 2.1, which is slightly higher than values (1.5–2.0) typically observed in incompressible turbulence (Wang *et al.* 1996). Figure 2 shows the compensated power spectra for the velocity field $\boldsymbol{u}$ and its two components $\boldsymbol{u}^s$ and $\boldsymbol{u}^c$. The energy spectra for $\boldsymbol{u}$ and $\boldsymbol{u}^s$ almost overlap, except at high wavenumbers where the compressive component dominates the energy content. The compensated energy
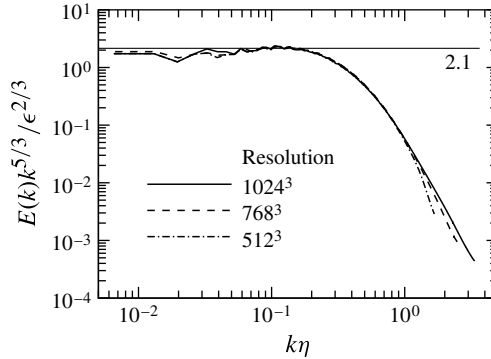
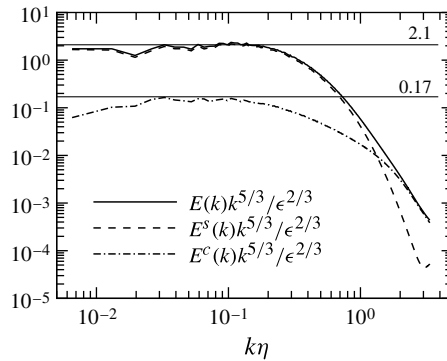FIGURE 1. Compensated energy spectra of the velocity field at three grid resolutions.

FIGURE 2. Compensated energy spectra for the velocity field and its two components.

level in the inertial subrange for the compressive component is roughly one order of magnitude smaller, but it decays much more slowly in the dissipative subrange.

The p.d.f.s of the normalized vorticity magnitude from three grid resolutions are shown in figure 3. The p.d.f.s of the vorticity magnitude for the 768^3 resolution and the 1024^3 resolution overlap almost everywhere. All of these p.d.f.s exhibit a well-defined exponential tail, qualitatively similar to the exponential tail of the vorticity magnitude p.d.f. reported for a similar turbulent Mach number (0.97) in Porter *et al.* (2002). A p.d.f. of the normalized vorticity magnitude (triangle) in an incompressible turbulent flow at Taylor Reynolds number $Re_\lambda = 168$ (Moisy & Jiménez 2004) is also plotted, where a longer stretched-exponential tail is observed. Donzis, Yeung & Sreenivasan (2008) indicate that the tail becomes longer as the Taylor Reynolds number is increased. We note that the Taylor Reynolds number in our simulation is $Re_\lambda = 254$, which is larger than $Re_\lambda = 168$ in the incompressible turbulent flow (Moisy & Jiménez 2004). Therefore, based on the comparison between two p.d.f.s in figure 3, we conclude that the intense vorticity is suppressed in the compressible turbulent flow, which is consistent with the observation in the weakly compressible turbulence (Miura 2004).

The p.d.f.s of the normalized dilatation from three grid resolutions are provided in figure 4. The p.d.f.s of the dilatation for the 768^3 and 1024^3 resolutions overlap almost
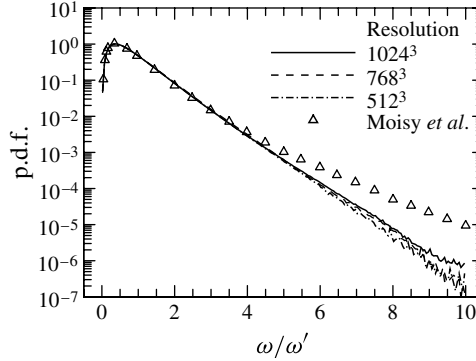
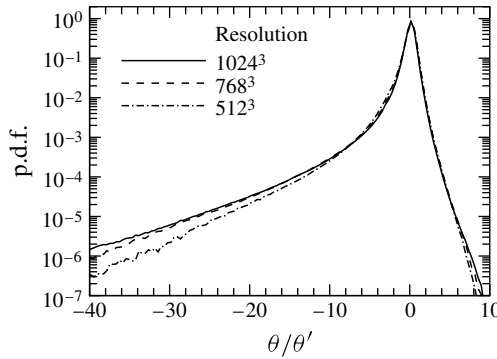FIGURE 3. The p.d.f.s of the normalized vorticity magnitude at three grid resolutions.

FIGURE 4. The p.d.f.s of the normalized dilatation at three grid resolutions.

everywhere, except for extremely strong compression regions ($\theta/\theta' < -30$). There is a strong tendency for the p.d.f. of the dilatation to be skewed to the negative value: the left tail of the p.d.f. falls very slowly, while its right tail is very short. The skewed shape for the p.d.f. of the dilatation has already been observed in weakly and moderately compressible turbulent flows (Porter *et al.* 2002; Pirozzoli & Grasso 2004). It was also shown in Pirozzoli & Grasso (2004) that the p.d.f. became more skewed towards the negative value as the turbulent Mach number was increased. Therefore, the p.d.f. of the dilatation in our simulated flow displays a longer left tail than others reported in previous simulations, due to the relatively higher turbulent Mach number and Taylor Reynolds number that we have achieved. A theoretical analysis of the left tail is provided separately to examine the similarities and differences between three-dimensional Navier–Stokes compressible turbulence and Burgers turbulence (Wang *et al.* 2012).

Here, we would like to emphasize that the results presented in this paper are not a direct numerical simulation study in some strict sense, since strong shocks with a thickness less than the grid length are certainly not directly resolved but modelled through numerical subgrid dissipation inherent in the WENO scheme. However, the fact that all dynamics are directly resolved in smooth regions makes our scheme essentially a direct numerical simulation for scales of the order of a few Kolmogorov
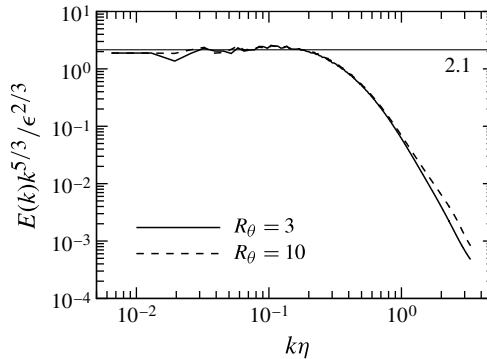
FIGURE 5. Compensated energy spectra of the velocity field for two different WENO region criteria, $R_\theta = -3$ and $R_\theta = -10$.

scales and larger. On the other hand, the WENO scheme introduces low-order errors at the shock front, and the errors at the shock front could propagate outside to potentially contaminate the bulk flow. That is exactly why we would like to carry out some careful grid refinement studies to ensure the convergence of small-scale statistics in our simulations.

Since the turbulent Mach number for the simulated flows in our study is not very high, many of the shocklets have finite thickness at the scales typically comparable to the Kolmogorov length scale (Samtaney *et al.* 2001). In order to resolve most of the shocklets, we simulated compressible turbulence with lower Taylor microscale Reynolds number compared to that in incompressible turbulence at the same grid resolution. The resolution parameter $k_{max}\eta$ in our simulation is ~ 3.33, much higher than $k_{max}\eta \approx 1.0$ which is required in direct numerical simulation of incompressible isotropic turbulence. For regions of strong shocklets that are not directly resolved, the conservation laws across the shocks are still exactly satisfied (WENO preserves shock relations). As indicated in Wang *et al.* (2010), as long as the thickness of the shocklets is kept reasonably small, the total amount of dissipation across the shocks is, for small viscosity, independent of viscosity, and dependent only on the jump conditions across the shocks. Therefore, while numerical viscosity smears the shock discontinuity (within 2–3 grid lengths), it does not alter the total amount of dissipation when integrated across the shock.

We note that in our hybrid method (Wang *et al.* 2010), the WENO scheme is used in the high compression regions according to a criterion $\theta/\theta' < -R_\theta$, where $R_\theta = 3$. To assess the effect of numerical dissipation by WENO, we have also performed a similar simulation with $R_\theta = 10$ in the 1024^3 grid resolution. The percentages of the WENO region in space are respectively 4.6 and 0.9 % for these two different criteria. We find that the energy spectra of the velocity field and the p.d.f.s of vorticity magnitude and dilatation for these two different criteria are closely matched (see figures 5–7), implying that general small-scale statistics are well resolved in the 1024^3 simulation presented in the paper.

4. Effect of dilatation on the vorticity and strain rate tensor

Our primary objectives are to study how the local compressibility alters the small-scale flow features relative to those of incompressible turbulence and to find
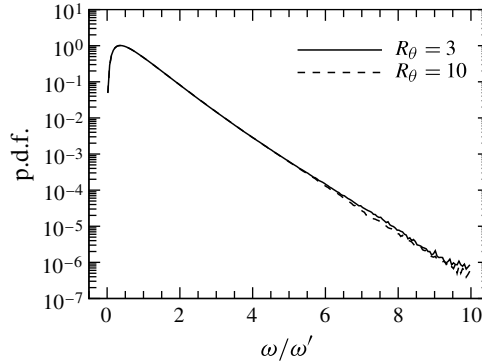
FIGURE 6. The p.d.f. of the normalized vorticity magnitude for two different WENO region criteria, $R_\theta = -3$ and $R_\theta = -10$.
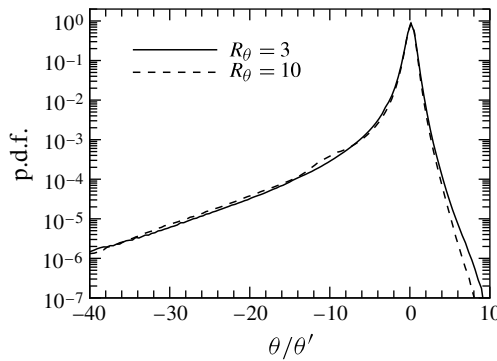

FIGURE 7. The p.d.f. of the normalized dilatation for two different WENO region criteria, $R_\theta = -3$ and $R_\theta = -10$.

ways to describe these alterations. To systematically quantify the effects of local compressibility, we divided the overall flow region into six subregions according to the level of local dilatation: (i) strong compression region with $\theta/\theta' \in [-\infty, -2.0]$; (ii) moderate compression region with $\theta/\theta' \in [-2.0, -1.0]$; (iii) weak compression region with $\theta/\theta' \in [-1.0, -0.0]$; (iv) weak expansion region with $\theta/\theta' \in [0.0, 1.0]$; (v) moderate expansion region with $\theta/\theta' \in [1.0, 2.0]$; (vi) strong expansion region with $\theta/\theta' \in [2.0, +\infty]$. Table 3 summarizes the percentage of spatial domain taken by each region. The weak compression and weak expansion regions occupy most volume in the flow field. The strong compression region (2.5 %) associated with shocks occurs much more frequently than the strong expansion region (0.2 %), and this is balanced by the more frequent appearance of the weak expansion region (57.8 %) when compared to the weak compression region (31.6 %). The moderate compression region and moderate expansion region each account for $\sim$4 % of the domain.

4.1. *Correlations of vorticity, dilatation and deviatoric strain rate tensor*

For the sake of clarifying the similarities to the incompressible turbulence, it is convenient to consider the deviatoric (or anisotropic) strain rate tensor $S_{ij}^* = S_{ij} - S_{kk}\delta_{ij}/3$ (Erlebacher & Sarkar 1993; Pirozzoli & Grasso 2004), where $S_{ij} = (\partial u_i/\partial x_j + \partial u_j/\partial x_i)/2$. By using the Helmholtz decomposition, the deviatoric strain

θ/θ'	$[-\infty, -2.0]$	$[-2.0, -1.0]$	$[-1.0, -0.0]$	$[0.0, 1.0]$	$[1.0, 2.0]$	$[2.0, +\infty]$
Fractions	2.5 %	4.2 %	31.6 %	57.8 %	3.7 %	0.2 %

TABLE 3. Percentage of volume occupied by flow regions with various dilatation levels.

	ω^2	$S_{ij}^* S_{ij}^*$	$S_{ij}^s S_{ij}^s$	$S_{ij}^{c*} S_{ij}^{c*}$
θ^2	0.012	0.79	0.006	0.97
ω^2	1.00	0.42	0.68	0.017

TABLE 4. Correlation factors between some pairs of variables relevant to the velocity gradients.

rate tensor is further decomposed into a solenoidal part and a compressive part (Erlebacher & Sarkar 1993): $S_{ij}^* = S_{ij}^s + S_{ij}^{c*}$. Then, the vortex stretching vector $W_i = \omega_j S_{ij}^*$ is decomposed as $W_i = W_i^s + W_i^c$, where $W_i^s = \omega_j S_{ij}^s$ and $W_i^c = \omega_j S_{ij}^{c*}$. Consequently, the enstrophy is governed by the following evolution equation (Erlebacher & Sarkar 1993):

$$\left(\frac{\partial}{\partial t} + u_j \frac{\partial}{\partial x_j}\right)\frac{\omega^2}{2} = \omega_i \omega_j S_{ij}^s + \omega_i \omega_j S_{ij}^{c*} - \frac{2}{3}\theta\omega^2 + \omega_i \frac{\epsilon_{ijk}}{\gamma M^2} \frac{1}{\rho^2} \frac{\partial \rho}{\partial x_j} \frac{\partial p}{\partial x_k}$$
$$+ \omega_i \frac{\epsilon_{ijk}}{Re} \frac{\partial}{\partial x_j} \left(\frac{1}{\rho} \frac{\partial \sigma_{mk}}{\partial x_m}\right), \tag{4.1}$$

where $\omega_i \omega_j S_{ij}^s$ and $\omega_i \omega_j S_{ij}^{c*}$ represent the vortex stretching or vortex compression by the solenoidal and compressive parts of the deviatoric strain rate tensor, respectively. The dilatational term $-(2/3)\theta\omega^2$ represents the direct effect of compression motions and expansion motions on enstrophy generation.

Erlebacher & Sarkar (1993) showed that in the compressible homogeneous turbulence, vorticity and dilatation are statistically independent. They further demonstrated the statistical correlation between vorticity and strain rate by calculating their correlation coefficient

$$\text{Corr}(f, g) = \frac{\langle (f - \langle f \rangle)(g - \langle g \rangle)\rangle}{\sqrt{\langle (f - \langle f \rangle)^2 \rangle \langle (g - \langle g \rangle)^2 \rangle}}, \tag{4.2}$$

where the angle brackets denote an ensemble average.

The corresponding correlation coefficients in our simulated flow are compiled in table 4. Indeed, the vorticity and dilatation, each derived respectively from the solenoidal part and the compressive part of the velocity, are nearly uncorrelated since the correlation coefficient between the squared dilatation and enstrophy is very small (0.012). The correlation coefficient between θ^2 and $S_{ij}^s S_{ij}^s$ is only 0.006. These results are in excellent agreement with the results of Erlebacher & Sarkar (1993), who found that the correlation coefficient between dilatation and any variable constructed from the solenoidal velocity was less than 0.01. We also observe that ω^2 (or θ^2) strongly correlates with $S_{ij}^s S_{ij}^s$ (or $S_{ij}^{c*} S_{ij}^{c*}$). Specifically, $\text{Corr}(\theta^2, S_{ij}^{c*} S_{ij}^{c*})$ is very close to 1.
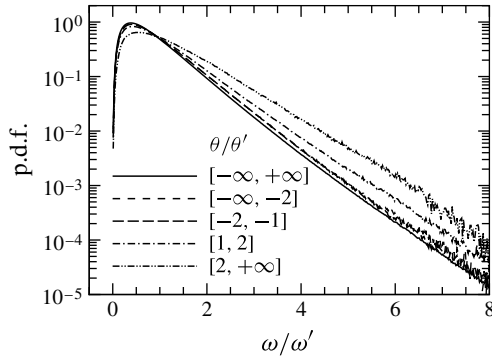
FIGURE 8. The p.d.f.s of the vorticity magnitude conditioned on the local dilatation.

To further examine the weak statistical dependence between vorticity and dilatation, we plot the p.d.f.s of vorticity magnitude conditioned on the local dilatation in figure 8. We find that with increasing dilatation in the expansion regions, the shape of the p.d.f. of vorticity magnitude becomes broader and the peak p.d.f. value drops slightly. This means some level of dependence of vorticity magnitude on the local dilatation. On the other hand, independence of the distribution of vorticity magnitude on dilatation was observed by Erlebacher & Sarkar (1993) in their simulations. The difference could be due to the much higher turbulent Mach number in our simulation relative to those in Erlebacher & Sarkar (1993). In fact, in our simulated flow, vorticity is substantially amplified when being advected through shocklets, leading to the concentration of intense vorticity downstream of the shocklets (Wang *et al.* 2011). In these regions, the flow is characterized by over-compression in shocklets, followed by an expansion downstream of the shocklets. In addition, as the strength of the shocklet is increased, both the expansion motion and the vorticity amplification increase downstream of the shocklet (Wang *et al.* 2011), leading to the positive correlation between dilatation and vorticity magnitude in high expansion regions.

In figure 9, the average vorticity magnitude conditioned on the local dilatation is plotted. It is clearly observed that the vorticity magnitude is independent of the local dilatation in the compression regions. However, the vorticity magnitude increases linearly with the dilatation in the expansion regions, yielding a small but positive correlation between the two. The behaviour of $S^s = \sqrt{S_{ij}^s S_{ij}^s}$ conditioned on θ is almost identical to that of the vorticity magnitude shown in figure 9. We therefore suspect that these features are shared by all small-scale variables constructed from the solenoidal component of the velocity field. In contrast, the conditional average of $S^{c*} = \sqrt{S_{ij}^{c*} S_{ij}^{c*}}$ is linearly dependent on the dilatation in both compression and expansion regions. Furthermore, the correlation is much stronger in compression regions than in the expansion regions.

4.2. *Dilatation effect on the enstrophy generation*

In compressible turbulence, local enstrophy generation includes contributions from the strain rate effect, dilatational effect and baroclinic effect. Wang *et al.* (2011) reported that the effect of the baroclinic term on enstrophy generation is negligible in a compressible isotropic turbulence at a similar turbulent Mach number. Therefore, the emphasis of our discussion will be placed on the strain rate term $\omega_i W_i$, the dilatation term $\omega_i W_i^D$, and their sum $\omega_i W_i^T$, where $W_i^D = -(2/3)\omega_i \theta$ and $W_i^T = \omega_j S_{ij}^* - (2/3)\omega_i \theta$.
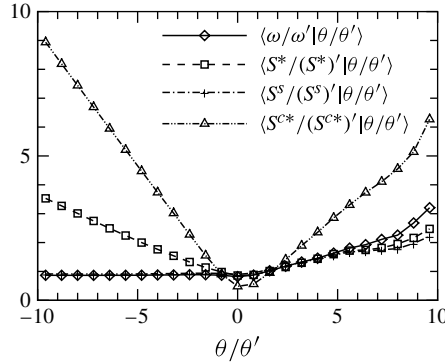
FIGURE 9. Average vorticity magnitude and strain rate conditioned on the dilatation.

Figure 10 shows average enstrophy generation $\omega_i W_i^T$ conditioned on the dilatation, as a function of the dilatation. It is found that in compression regions, $\omega_i W_i^T$ is always positive and increases linearly as dilatation is decreased, implying enhancement of enstrophy generation by compression motions. However, in strong expansion regions, $\omega_i W_i^T$ becomes negative and decreases drastically as dilatation is increased, implying massive destruction of enstrophy by strong expansion motions. To connect the dilatational effect on enstrophy generation with the shocklets effect discussed in Wang *et al.* (2011), we introduce the direction of density gradient as

$$n_i = \frac{\partial \rho / \partial x_i}{\sqrt{(\partial \rho / \partial x_1)^2 + (\partial \rho / \partial x_2)^2 + (\partial \rho / \partial x_3)^2}}. \tag{4.3}$$

Normal and tangential components of vorticity relative to the local density isosurface are defined by $\omega_{n,i} = (\omega_j n_j) n_i$ and $\omega_{t,i} = \omega_i - (\omega_j n_j) n_i$, respectively. Similarly, W^T is decomposed into a normal component $W_{n,i}^T$ and a tangential component $W_{t,i}^T$. Figure 10 shows the conditional average of both normal and tangential components of enstrophy generation. The normal component of enstrophy generation is negligible as compared to its tangential counterpart in both strong compression regions and strong expansion regions. Since the normal direction of a shocklet (in strong compression regions) is aligned with the density gradient, the above observations are consistent with the result that only the tangential component of the vorticity is increased across the shocklet (Wang *et al.* 2011).

Figure 11 shows the conditional average of dilatational enstrophy generation $\omega_i W_i^D = -(2/3)\theta \omega^2$ and its two components $\omega_{n,i} W_{n,i}^D = -(2/3)\theta \omega^2 \cos^2(\boldsymbol{n}, \boldsymbol{\omega})$ and $\omega_{t,i} W_{t,i}^D = -(2/3)\theta \omega^2 \sin^2(\boldsymbol{n}, \boldsymbol{\omega})$. The direct interaction between dilatation and vorticity is isotropic, and negative (or positive) dilatation makes positive (or negative) contributions to enstrophy generation. In expansion regions, $\omega_i W_i^D$ decreases quickly as dilatation becomes larger due to positive correlation between enstrophy and dilatation in these regions. In the inset of figure 11 we plot average $\cos^2(\boldsymbol{n}, \boldsymbol{\omega})$ conditioned on the dilatation. The average $\cos^2(\boldsymbol{v}, \boldsymbol{w})$ is equal to $1/3$ if the two vectors $\boldsymbol{v}$ and $\boldsymbol{w}$ are distributed independently. We found that the average $\cos^2(\boldsymbol{n}, \boldsymbol{\omega})$ is smaller than $1/3$ in both compression regions and expansion regions. Thus, there is a tendency for vorticity to be perpendicular to the density gradient, consistent with the previous observation that the tangential component of the overall enstrophy generation dominates over its normal counterpart. Consequently, the average value of the tangential
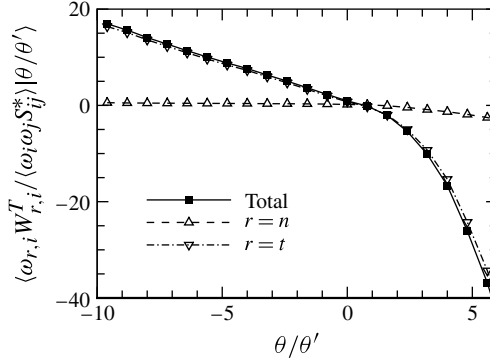
FIGURE 10. Averages of $\omega_i W_i^T$, $\omega_{n,i} W_{n,i}^T$ and $\omega_{t,i} W_{t,i}^T$ conditioned on the dilatation.
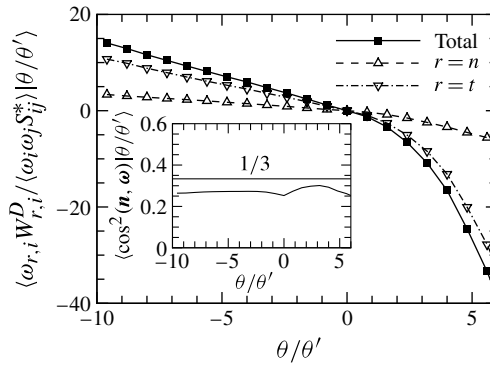

FIGURE 11. Averages of $\omega_i W_i^D$, $\omega_{n,i} W_{n,i}^D$ and $\omega_{t,i} W_{t,i}^D$ conditioned on the dilatation.

component $\omega_{t,i} W_{t,i}^D$ of dilatational enstrophy generation is more than twice its normal counterpart, as shown in figure 11.

After briefly discussing the effect of the dilatational term $-(2/3)\theta\omega^2$ on enstrophy generation, we shall now focus on enstrophy generation by the deviatoric strain rate tensor via the vortex stretching and tilting mechanism. In incompressible turbulence, the predominance of vortex stretching over vortex compression and the dynamic alignment between the vorticity and vortex stretching vector cause self-amplification of local vorticity and redistribution of vorticity over smaller scales (Galanti & Tsinober 2000; Kholmyansky *et al.* 2001). Consequently, $\omega_i \omega_j S_{ij}^*$ is the positive production term in the enstrophy equation. For compressible turbulence, we must consider the effects of dilatation. Figure 12 shows average $\omega_i W_i = \omega_i \omega_j S_{ij}^*$ conditioned on the dilatation, as a function of the dilatation. We find that the magnitude of $\omega_i \omega_j S_{ij}^*$ increases roughly linearly with the level of dilatation in compression regions. In expansion regions, $\omega_i \omega_j S_{ij}^*$ shows rather complicated variations: it first increases with dilatation, then decreases from positive to highly negative. Therefore, the compression enhances the production of enstrophy from the vortex stretching term $\omega_i \omega_j S_{ij}^*$. But high expansion weakens this production mechanism, and in extreme expansion regions, $\omega_i \omega_j S_{ij}^*$ can even become a destruction term for enstrophy. Furthermore, in high compression regions, the normal component $\omega_{n,i} W_{n,i}$ of the vortex stretching term is
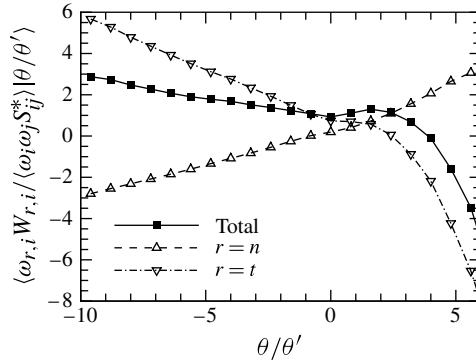
FIGURE 12. Averages of $\omega_i W_i$, $\omega_{n,i} W_{n,i}$ and $\omega_{t,i} W_{t,i}$ conditioned on the dilatation.
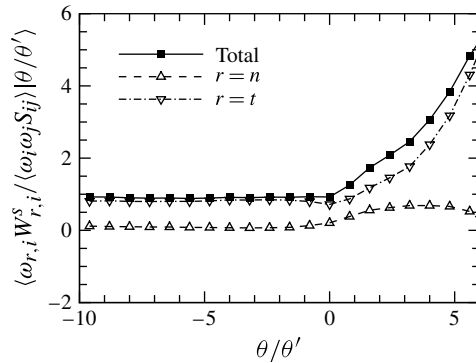

FIGURE 13. Averages of $\omega_i W_i^s$, $\omega_{n,i} W_{n,i}^s$ and $\omega_{t,i} W_{t,i}^s$ conditioned on the dilatation.

negative, leading to substantial destruction of enstrophy. The negative average value of $\omega_{n,i} W_{n,i}$ also balances positive contributions from the normal component $\omega_{n,i} W_{n,i}^D$ of the dilatational enstrophy generation in high compression regions. In expansion regions, the average $\omega_{n,i} W_{n,i}$ makes significant positive contributions to enstrophy generation. These observations will be further investigated via the strain rate tensor later in the paper.

Interestingly, figure 13 shows that the solenoidal vortex stretching term $\omega_i W_i^s = \omega_i \omega_j S_{ij}^s$ is not affected by compression motions. The effect of expansion motions is to enlarge $\omega_i \omega_j S_{ij}^s$. These features are similar to those of the conditional average of vorticity magnitude and the solenoidal strain rate. In addition, the average value of the normal component $\omega_{n,i} W_{n,i}^s$ is small compared to its tangential component. Otherwise, according to figure 14, the compressive component of the vortex stretching term is enhanced by compression motions, which is the reason for the overall enhancement of the enstrophy production of $\omega_i \omega_j S_{ij}^*$. In expansion regions, the conditional average of $\omega_i \omega_j S_{ij}^{c*}$ is always negative, and its magnitude increases rapidly with the dilatation. The magnitude of the conditional average of $\omega_i \omega_j S_{ij}^{c*}$ exceeds that of $\omega_i \omega_j S_{ij}^s$ starting at $\theta/\theta' = 4$, leading to the net destruction of enstrophy by the term $\omega_i \omega_j S_{ij}^*$ for $\theta/\theta' > 4$. Furthermore, in both compression and expansion regions, the average value of the normal component $\omega_{n,i} W_{n,i}^c$ is significant, and plays the opposite role in enstrophy generation as compared to its tangential counterpart.
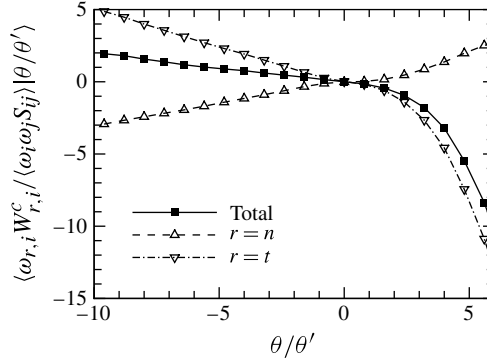
FIGURE 14. Averages of $\omega_i W_i^c$, $\omega_{n,i} W_{n,i}^c$ and $\omega_{t,i} W_{t,i}^c$ conditioned on the dilatation.

Figure 15 shows the average enstrophy generation terms $\omega_i W_i^T$, $\omega_i W_i^D$ and $\omega_i W_i$ conditioned on the dilatation at three grid resolutions. There is a substantial deviation of the average values for the 512^3 resolution from those for the 1024^3 resolution where dilatation magnitude is large. However, the difference of average values from the 768^3 resolution and the 1024^3 resolution is small in almost all ranges of dilatation shown in the figure, implying the convergence of enstrophy generation under this grid refinement.

In figure 16 we plot the p.d.f. and conditional p.d.f.s of the cosine of the angle between vorticity and the vortex stretching vector W_i. Similar to the case of incompressible turbulence (Kholmyansky *et al.* 2001), there is a definite positive alignment between the vorticity and the vortex stretching vector. In addition, this alignment is somewhat enhanced by compression and is significantly reduced by expansion. Figure 17 shows that the effect of the dilatation on the alignment between vorticity and the solenoidal vortex stretching vector is negligible, and only strong expansion slightly weakens this alignment.

The alignment between the vorticity and the vortex stretching vector associated with the compressive velocity component is displayed in figure 18, showing that the effect of dilatation is significant. Without conditioning on the dilatation, there is no clear alignment of $\boldsymbol{\omega}$ and $\boldsymbol{W}^c$. Parallel alignment is observed for $\theta < 0$, and this alignment is enhanced as the compression is increased. For expansion regions, a tendency for anti-parallel alignment between $\boldsymbol{\omega}$ and $\boldsymbol{W}^c$ is observed, which is responsible for the weakening of enstrophy production from the vortex stretching term.

In figure 19, the isosurfaces of dilatation at $\theta = -3\theta'$ and $\theta = \theta'$ are displayed in a 256^3 subdomain (i.e. 1/64 of the full domain). These isosurfaces are coloured based on the local enstrophy production of the deviatoric strain rate $\omega_i \omega_j S_{ij}^*$ and its solenoidal and compressive components. At $\theta = -3\theta'$, the isosurfaces are random sheet-like shock waves of a thickness typically smaller than the inertial subrange scales. The width of these shock fronts spans over a wide scale range. The local enstrophy production of the deviatoric strain rate tensor $\omega_i \omega_j S_{ij}^*$ is typically positive on these shock fronts. After the Helmholtz decomposition, it is observed that the compressive component of the deviatoric strain rate makes more contributions to the local enstrophy production or destruction than its solenoidal component. Still, the solenoidal component of the deviatoric strain rate tensor is more likely to produce the enstrophy than to destroy it. In contrast, the expansion regions formed by $\theta = \theta'$
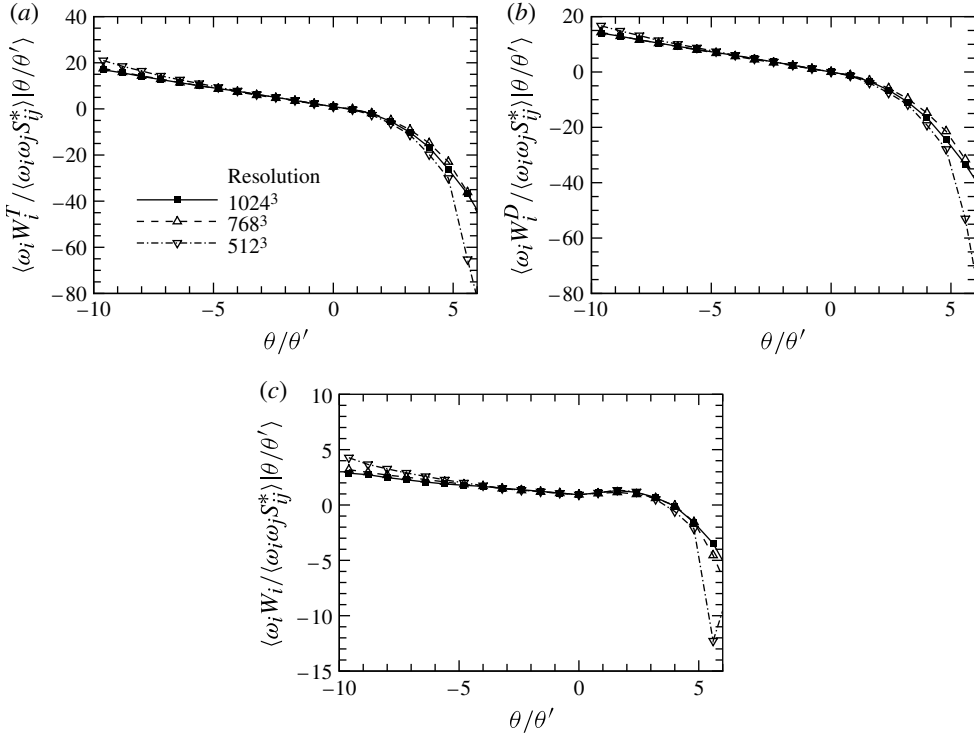
FIGURE 15. Averages of $\omega_i W_i^T$, $\omega_i W_i^D$ and $\omega_i W_i$ conditioned on the dilatation for three different grid resolutions.
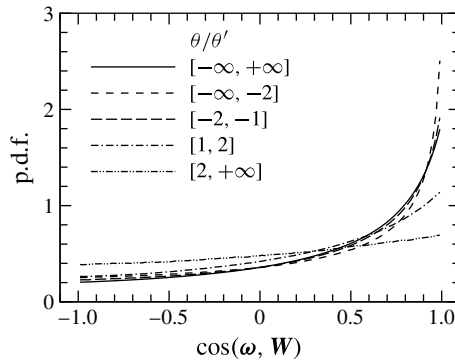

FIGURE 16. The p.d.f. and conditional p.d.f.s of the cosines of the angle between vorticity $\boldsymbol{\omega}$ and the vortex stretching vector $\boldsymbol{W}$.

take blob- or tube-like structures. The length scales of these expansion structures are relatively small when compared to the shock waves. In addition, many of the structures resemble the shape of vortex tubes familiar from incompressible turbulence. After the Helmholtz decomposition, it is revealed that, in these expansion regions, the solenoidal component of the deviatoric strain rate contributes mostly to strong
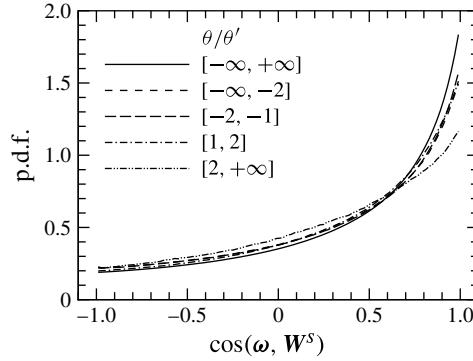
FIGURE 17. The p.d.f. and conditional p.d.f.s of the cosines of the angle between vorticity $\boldsymbol{\omega}$ and the solenoidal vortex stretching vector $\boldsymbol{W}^s$.
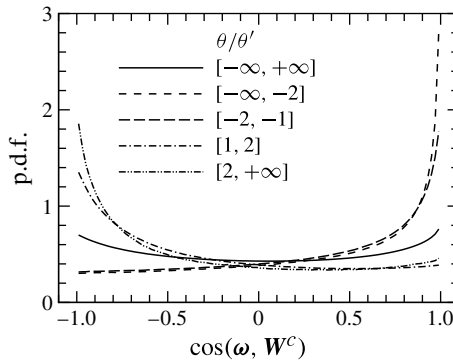

FIGURE 18. The p.d.f. and conditional p.d.f.s of the cosines of the angle between vorticity $\boldsymbol{\omega}$ and the compressive vortex stretching vector $\boldsymbol{W}^c$.

enstrophy production, but the compressive component of the deviatoric strain rate gives rise mostly to enstrophy destruction.

4.3. *Dilatation effect on the strain rate tensor*

Let the three eigenvectors of the strain rate tensor S_{ij} be denoted by $\boldsymbol{\Lambda}_1$, $\boldsymbol{\Lambda}_2$ and $\boldsymbol{\Lambda}_3$, with corresponding eigenvalues λ_1, λ_2 and λ_3, arranged in ascending order, i.e. $\lambda_1 \leqslant \lambda_2 \leqslant \lambda_3$. Then the three eigenvectors of the deviatoric part of strain rate tensor S_{ij}^* are $\boldsymbol{\Lambda}_1$, $\boldsymbol{\Lambda}_2$ and $\boldsymbol{\Lambda}_3$ respectively, and the corresponding eigenvalues are $\lambda_k^* = \lambda_k - \theta/3$ ($k = 1, 2, 3$). The eigenvalues λ_k^* satisfy the following condition as in incompressible turbulence:

$$\lambda_1^* + \lambda_2^* + \lambda_3^* = 0. \tag{4.4}$$

Figure 20 displays the p.d.f.s and conditional p.d.f.s of the normalized eigenvalues β_k of the strain rate tensor S_{ij}, where

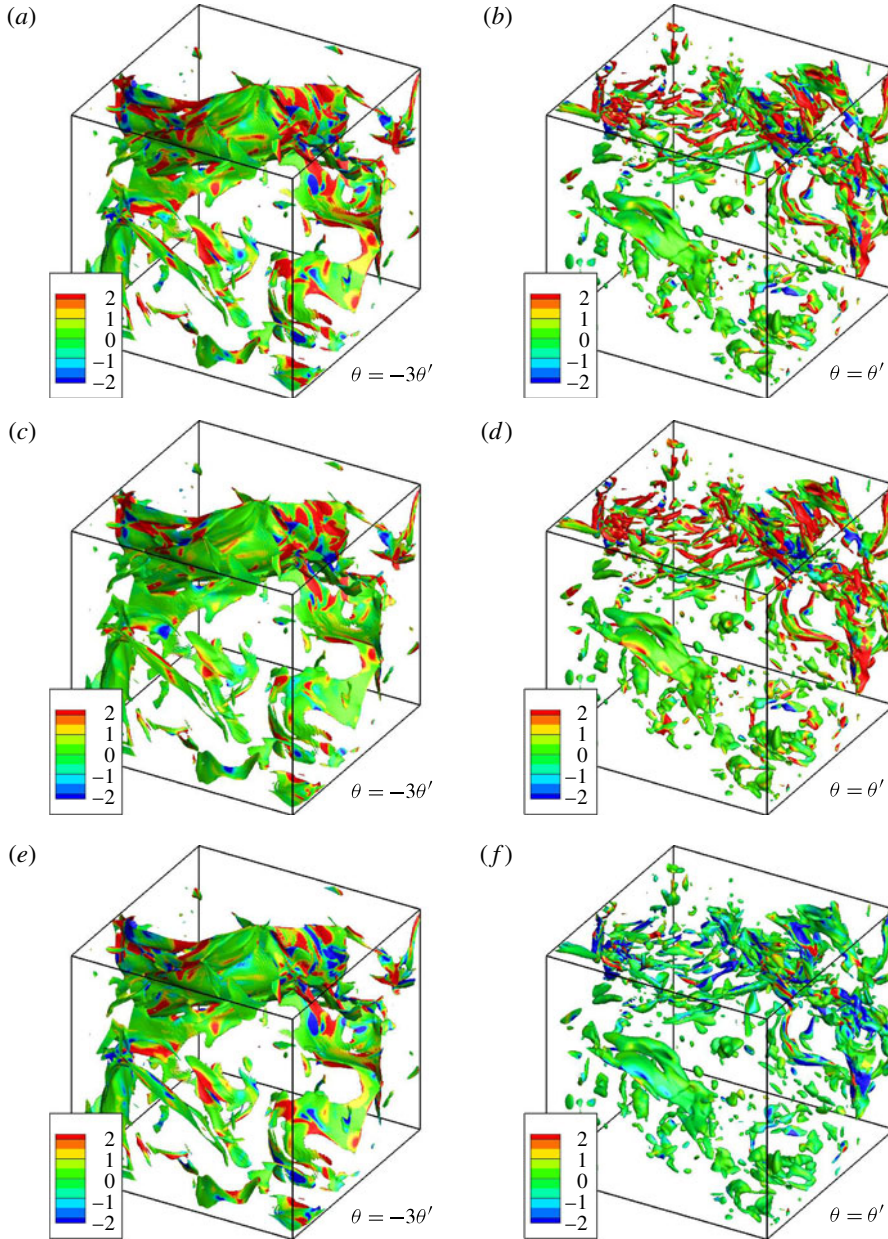$$\beta_k = \frac{\lambda_k}{\sqrt{\lambda_1^2 + \lambda_2^2 + \lambda_3^2}}. \tag{4.5}$$

FIGURE 19. Isosurfaces of dilatation at $\theta = -3\theta'$ and $\theta = \theta'$ in a 256^3 subdomain covering $(242\eta)^3$. The isosurfaces are coloured by (a,b) $\omega_i\omega_j S_{ij}^*/\langle\omega_i\omega_j S_{ij}^*\rangle$, (c,d) $\omega_i\omega_j S_{ij}^s/\langle\omega_i\omega_j S_{ij}^*\rangle$, and (e,f) $\omega_i\omega_j S_{ij}^{c*}/\langle\omega_i\omega_j S_{ij}^*\rangle$.

In the overall flow field, the most probable eigenvalue ratio for the strain rate tensor is $-3:1:2.5$, quantitatively different from the preferred eigenvalue ratio of $-4:1:3$ reported in incompressible turbulence (Ashurst *et al.* 1987) and weakly compressible turbulence (Erlebacher & Sarkar 1993; Pirozzoli & Grasso 2004; Lee *et al.* 2009). In compression regions, the peak value of the p.d.f. of β_2 shifts to the left side as the
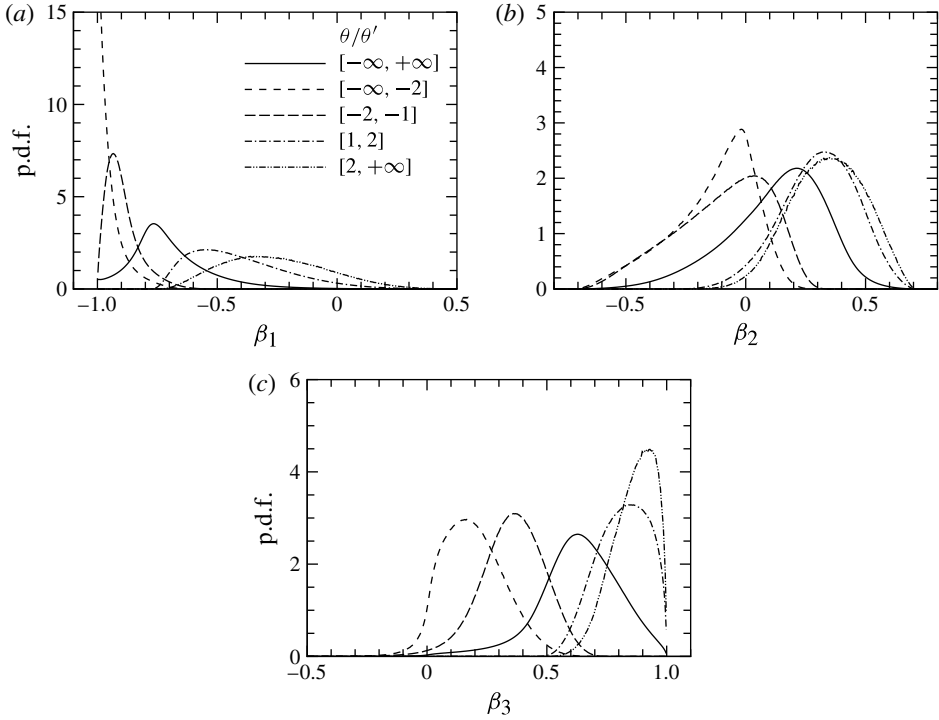
FIGURE 20. The p.d.f.s and conditional p.d.f.s of the normalized eigenvalues of the strain rate tensor S_{ij}.

compression level increases. In high compression regions, values of both β_2 and β_3 are very small compared to the value of β_1, and the p.d.f. of β_1 has a peak value very close to -1. Therefore, most of the eigenvalue ratios are approximately $-1:0:0$ in high compression regions, implying that strong compression regions are dominated by sheet-like structures (i.e. shocklets). On the other hand, in strong expansion regions, the peak value of the p.d.f. of β_3 is located near 1, indicating that the local expansion motion along the third strain rate eigenvector is dominant.

Figure 21(a) shows the p.d.f.s and conditional p.d.f.s of the ratio λ_2^s/λ_1^s of the intermediate to the minimum eigenvalues of the solenoidal strain rate tensor S_{ij}^s. This ratio peaks at $\lambda_2^*/\lambda_1^* = -0.27$, corresponding to the most likely eigenvalue ratio of $-3.7:1:2.7$, in good agreement with the result of $-4:1:3$ in incompressible turbulence (Ashurst *et al.* 1987). In addition, the p.d.f. shape of λ_2^s/λ_1^s is barely changed by dilatation, except that strong expansion motions slightly broaden this p.d.f. shape and shift the peak location to the right. Figure 21(b–d) displays p.d.f.s and conditional p.d.f.s of the normalized eigenvalues β_k^c of the compressive strain rate tensor S_{ij}^c. In strong compression regions, the p.d.f. shape of β_1^c becomes rather sharp, so that almost all of the ratios $\beta_1^c:\beta_2^c:\beta_3^c$ concentrate near $-1:0:0$, demonstrating sheet-like structures of compressive velocity component generated by intensive compression motions. On the other hand, in strong expansion regions, the peak value of the p.d.f. of β_2^c is close to 0.5, far from zero, implying that strong expansion motions are multidirectional. Due to distinctive properties of β_k^c in compression and expansion regions, the p.d.f. shape of β_k^c for the overall flow field is very broad and complicated.
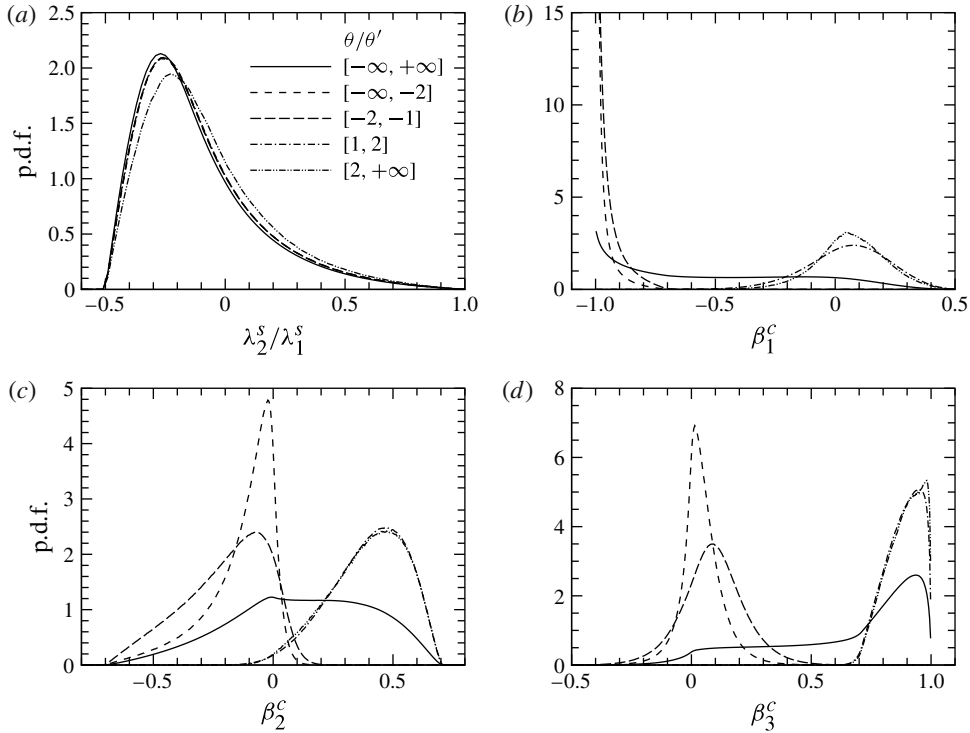
FIGURE 21. The p.d.f.s and conditional p.d.f.s of the ratios of the intermediate to the minimum eigenvalues of the solenoidal strain rate tensor S_{ij}^s, and the p.d.f.s and conditional p.d.f.s of the normalized eigenvalues of the compressive strain rate tensor S_{ij}^c.

Figure 22 shows the conditional averages of squares of cosines of angles between density gradient and eigenvectors of the strain rate tensor $\boldsymbol{\Lambda}_k$, $\boldsymbol{\Lambda}_k^s$ and $\boldsymbol{\Lambda}_k^c$. The conditional average value of $\cos^2(\boldsymbol{n}, \boldsymbol{\Lambda}_1)$ approaches 1 with the increase of compression level, indicating that the eigenvector corresponding to the most negative eigenvalue of strain rate tensor tends to be aligned with the density gradient in high compression regions. In fact, in the vicinity of a shocklet, both the density gradient and the first strain rate eigenvector are perpendicular to the shock surface (Wang *et al.* 2011). In expansion regions, there are obvious tendencies for the third strain rate eigenvector to be aligned with the density gradient and the first strain rate eigenvector to be perpendicular to the density gradient. These trends are more obvious for the eigenvectors of the compressive-velocity-component strain rate tensor as shown in figure 22(*c*). For the solenoidal-velocity-component strain rate tensor, the conditional average values of $\cos^2(\boldsymbol{n}, \boldsymbol{\Lambda}_k^s)$ ($k = 1, 2, 3$) are close to $1/3$, indicating that the alignments between these eigenvectors and the density gradient are not clear.

In terms of the eigenvalues of the deviatoric strain rate tensors and the cosines of angles between the vorticity and the eigenvectors, the vortex stretching terms can be written as

$$\omega_i \omega_j S_{ij}^* = \omega^2 \left[\lambda_1^* \cos^2(\boldsymbol{\Lambda}_1, \boldsymbol{\omega}) + \lambda_2^* \cos^2(\boldsymbol{\Lambda}_2, \boldsymbol{\omega}) + \lambda_3^* \cos^2(\boldsymbol{\Lambda}_3, \boldsymbol{\omega}) \right], \quad (4.6)$$

$$\omega_i \omega_j S_{ij}^s = \omega^2 \left[\lambda_1^s \cos^2(\boldsymbol{\Lambda}_1^s, \boldsymbol{\omega}) + \lambda_2^s \cos^2(\boldsymbol{\Lambda}_2^s, \boldsymbol{\omega}) + \lambda_3^s \cos^2(\boldsymbol{\Lambda}_3^s, \boldsymbol{\omega}) \right], \quad (4.7)$$

$$\omega_i \omega_j S_{ij}^{c*} = \omega^2 \left[\lambda_1^{c*} \cos^2(\boldsymbol{\Lambda}_1^c, \boldsymbol{\omega}) + \lambda_2^{c*} \cos^2(\boldsymbol{\Lambda}_2^c, \boldsymbol{\omega}) + \lambda_3^{c*} \cos^2(\boldsymbol{\Lambda}_3^c, \boldsymbol{\omega}) \right]. \quad (4.8)$$
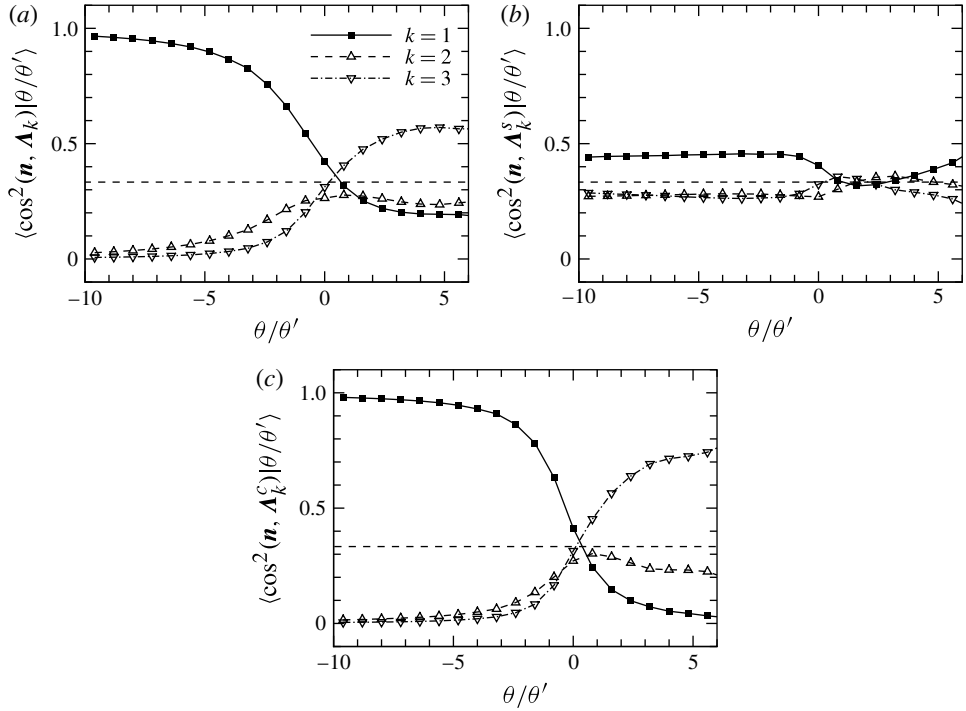
FIGURE 22. Conditional averages of squares of cosines of angles between density gradient and eigenvectors of the strain rate tensor Λ_k, Λ_k^s and Λ_k^c. The horizontal line at $1/3$ represents the average value for two randomly distributed vectors.

These equations show that the first eigenvalue always makes a negative contribution to the enstrophy production, while the third eigenvalue always makes a positive contribution to the enstrophy production. The role of the second eigenvalue depends on its sign and magnitude. In incompressible turbulence, it is known to be positively skewed, leading to net enstrophy production. In addition, the orientations of vorticity relative to the strain rate eigenvectors are also essential to the enstrophy production. The tendency of the vorticity to be aligned with the second eigenvector causes a substantial enstrophy production in incompressible turbulence. In the following discussions, we shall first examine the local compressibility effect on the alignment statistics between vorticity and strain rate eigenvectors. Then we investigate the statistical properties of the strain rate eigenvalues. Finally, we will combine these results together to quantify the contributions to the enstrophy production of the vortex stretching along each principal direction of the strain rate tensor, at different dilatation levels.

Figure 23 shows alignment statistics between the vorticity and strain rate eigenvectors, conditioned on the local dilatation. The overall alignment behaviours of the vorticity relative to the strain rate eigenvectors are quite similar to those found in the incompressible turbulence (Ashurst *et al.* 1987; Galanti & Tsinober 2000; Kholmyansky *et al.* 2001) and in the weakly compressible turbulence (Erlebacher & Sarkar 1993; Pirozzoli & Grasso 2004; Lee *et al.* 2009): (i) there is a strong tendency for the vorticity to align with the intermediate eigenvector; (ii) there is also a noticeable tendency for vorticity to be perpendicular to the first eigenvector
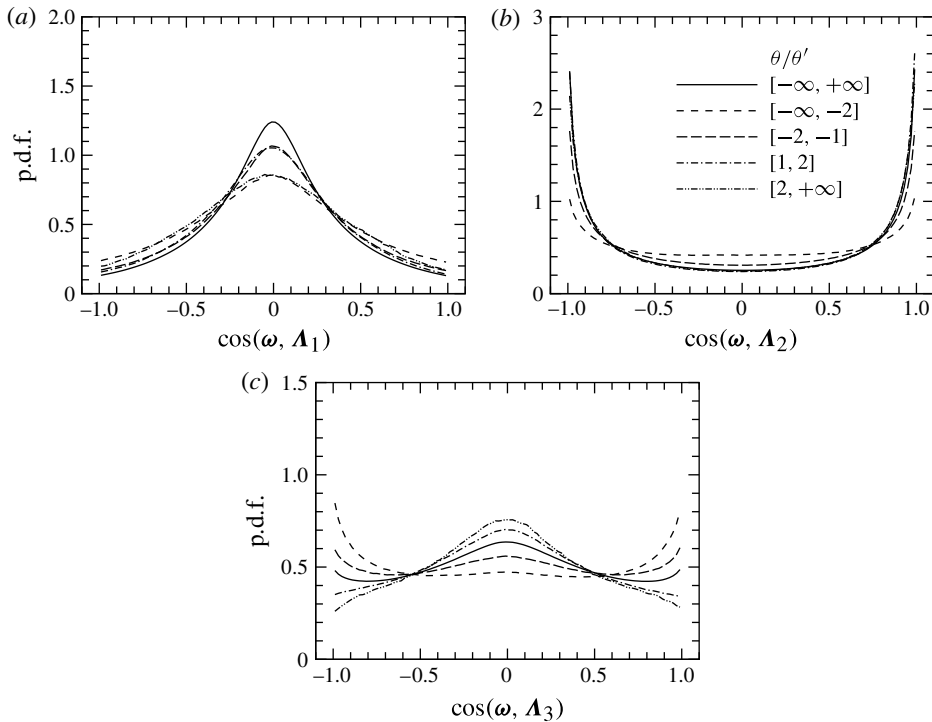
FIGURE 23. The p.d.f.s and conditional p.d.f.s of the cosines of the angle between vorticity $\boldsymbol{\omega}$ and the eigenframe $\boldsymbol{\Lambda}_i$.

corresponding to the most negative eigenvalue; (iii) the distribution of the angle between the vorticity and the third eigenvector (the one with the most positive eigenvalue) is almost uniform. In our simulated highly compressible turbulence, we observe diverse influences of the dilatation on the angle of vorticity relative to different eigenvectors. For the first strain rate eigenvector, positive or negative dilatation both weaken its perpendicular alignment with vorticity. The effect of positive dilatation on the alignment between the vorticity and the intermediate eigenvector is negligible while the negative dilatation substantially weakens this alignment. Furthermore, as the dilatation shifts from negative to positive, the alignment between the vorticity and the third eigenvector changes from being more likely parallel to somewhat perpendicular.

After performing the Helmholtz decomposition, we found that there is a negligible effect of the dilatation on the angle between the vorticity and the solenoidal-velocity-component strain rate eigenvectors. The alignments between the vorticity and this solenoidal strain rate eigenvectors are identical to that of incompressible turbulence. Therefore, the geometrical statistics of the solenoidal component of the turbulent flow is insensitive to the local compressibility effect in our simulated flow. However, for the angle between the vorticity and the compressive-velocity-component strain rate eigenvectors, the most remarkable feature is that high expansion causes $\boldsymbol{\omega}$ to be strongly aligned with $\boldsymbol{\Lambda}_1^c$ and perpendicular to $\boldsymbol{\Lambda}_2^c$.

Average eigenvalues of the deviatoric strain rate tensor conditioned on the dilatation are plotted in figure 24. In strong compression regions, the magnitude of the first
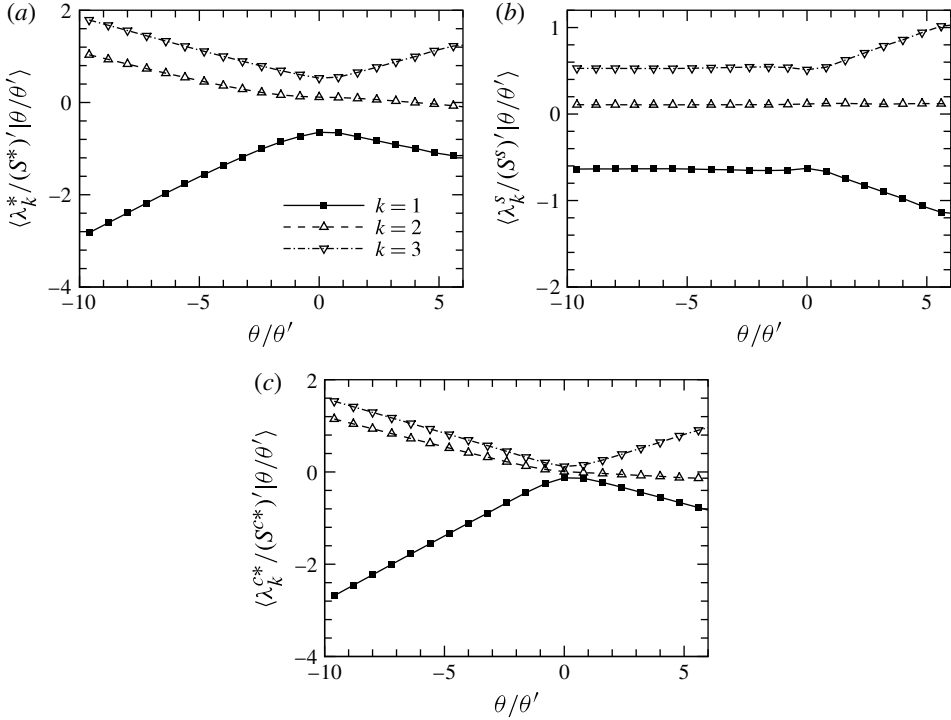
FIGURE 24. Average eigenvalues of the deviatoric strain rate tensor S_{ij}^*, S_{ij}^s and S_{ij}^{c*} conditioned on the dilatation.

(smallest) eigenvalue is much larger than either of the other two eigenvalues. In expansion regions, as the dilatation increases, the first and third eigenvalues increase simultaneously, while the magnitude of the intermediate eigenvalue remains relatively small. The eigenvalue ratio approaches -1:0:1 in strong expansion regions. Although relatively small, the intermediate eigenvalue is essential in determining the enstrophy production by vortex stretching. Betchov (1956) proved that in incompressible flow, the positive sign of the intermediate eigenvalue of the strain rate tensor is necessary for $\omega_i \omega_j S_{ij}^*$ to produce enstrophy. In our simulation, the conditional mean of the intermediate eigenvalue decreases monotonically, from being positive to negative, as the dilatation is increased. The zero crossing occurs at $\theta/\theta' \approx 4$, precisely where the conditional mean of $\omega_i \omega_j S_{ij}^*$ changes its sign (from being a production term to a destruction term). This coincidence further stresses the important role played by the intermediate eigenvalue.

After the decomposition, we find that expansion motions enlarge the minimum and maximum eigenvalues of the solenoidal deviatoric strain rate tensor, while the intermediate eigenvalue is unchanged by the increasing dilatation. For the compressive component, the conditional mean of the intermediate eigenvalue λ_2^{c*} changes from a positive value to a negative value when the dilatation is changed from negative to positive. The conditional average of eigenvalue ratio λ_1^{c*}:λ_2^{c*}:λ_3^{c*} changes from close to -2:1:1 when $\theta < 0$ to roughly -1:0:1 when $\theta > 0$.

In figure 25(a) we plot the conditional averages of $\cos^2(\omega, \Lambda_k)$. We note that the average of $\cos^2(v, w)$ is equal to $1/3$ if the two vectors v and w are distributed independently and uniformly. When $\theta > 0$, $\cos^2(\omega, \Lambda_2)$ is nearly constant and is
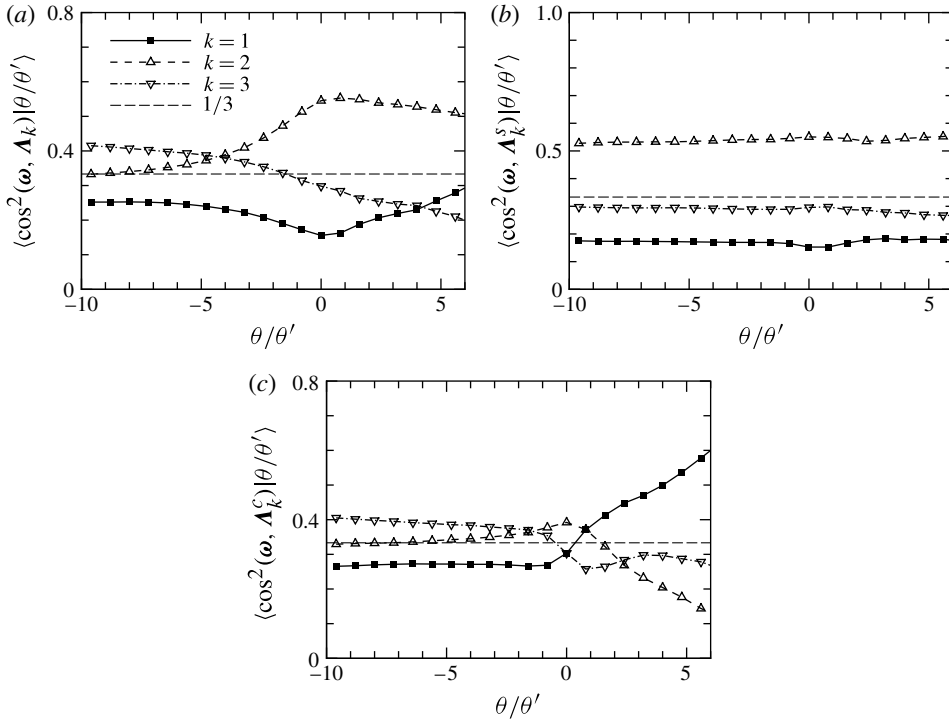
FIGURE 25. Conditional averages of squares of cosines of angles between vorticity and eigenvectors of the strain rate tensor Λ_k, Λ_k^s and Λ_k^c. The horizontal line at $1/3$ represents the average value for two randomly distributed vectors.

significantly larger than $1/3$, consistent with the result of figure 23(b) that the alignment between ω and Λ_2 is not affected by expansion. Therefore, the contribution to the enstrophy production by the second strain rate eigenvector, $\omega^2\lambda_2^*\cos^2(\Lambda_2, \omega)$, is significant (see figure 26a) in the expansion regions, even though the magnitude of the second strain rate eigenvalue is quite small. When $\theta < 0$, as the compression rate increases, $\cos^2(\omega, \Lambda_2)$ decreases, implying that the alignment between ω and Λ_2 is weakened by compression, as clearly shown in figure 23. Nevertheless, $\omega^2\lambda_2^*\cos^2(\Lambda_2, \omega)$ is still amplified by compression due to the enlarged second strain rate eigenvalue. In the weak compression and weak expansion regions, we find that $\omega^2\lambda_2^*\cos^2(\Lambda_2, \omega)$ is comparable to or even slightly larger than $\omega^2\lambda_3^*\cos^2(\Lambda_3, \omega)$. In contrast, in the strong expansion or strong compression regions, the third eigenvector corresponding to the largest positive eigenvalue makes the dominant contribution to the enstrophy production.

Figure 25(b) provides the conditional average of $\cos^2(\omega, \Lambda_k^s)$. This figure demonstrates again that the angles between the vorticity and the solenoidal strain rate eigenvectors are insensitive to the change of the dilatation. Another interesting observation is that the enstrophy production by the second solenoidal strain rate eigenvalue is always comparable to that by the third solenoidal strain rate eigenvalue (see figure 26b). Specifically, as the expansion level increases, the average $\omega^2\lambda_2^s\cos^2(\Lambda_2^s, \omega)$ also increases. Since both λ_2^s and $\cos^2(\omega, \Lambda_2^s)$ remain nearly constant, this enhancement of enstrophy production is ascribed primarily to the more intensive vorticity field in the expansion regions.
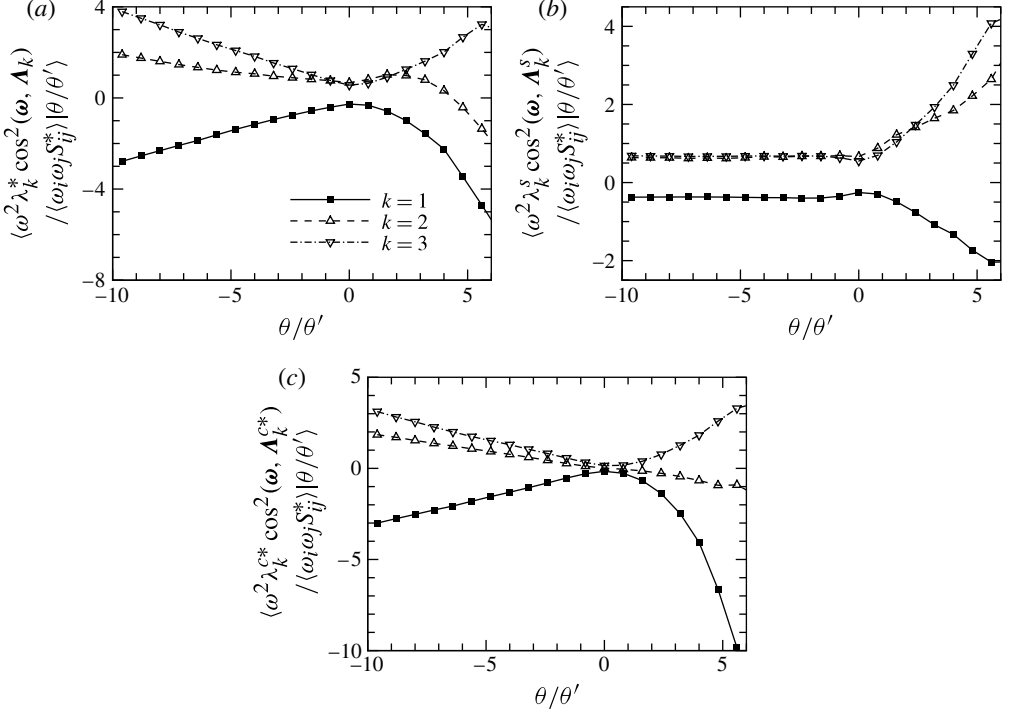
FIGURE 26. Conditional averages of enstrophy production by the three eigenvectors of the deviatoric strain rate tensor Λ_k, Λ_k^s and Λ_k^c.

Finally, figure 25(c) shows the conditional average of $\cos^2(\boldsymbol{\omega}, \Lambda_k^c)$. In the compression regions, $\cos^2(\boldsymbol{\omega}, \Lambda_k^c)$ are close to $1/3$, the value for a random field. As the expansion level increases, $\cos^2(\boldsymbol{\omega}, \Lambda_1^c)$ increases rapidly, indicating a strong tendency for the vorticity to be aligned with the first compressive strain rate eigenvector in the strong expansion regions. Therefore, the magnitude of average $\omega^2 \lambda_1^{c*} \cos^2(\Lambda_1^c, \boldsymbol{\omega})$ is much larger than that of average $\omega^2 \lambda_3^{c*} \cos^2(\Lambda_3^c, \boldsymbol{\omega})$ (see figure 26c) in the strong expansion regions.

In order to include the effect of the dilatational term on the enstrophy generation, we define the modified eigenvalues ζ_k of the strain rate tensor as $\zeta_k = \lambda_k - \theta$ according to the equation $\omega_i \omega_j S_{ij}^* - (2/3)\theta \omega^2 = \omega_i \omega_j (S_{ij} - \delta_{ij}\theta)$. Consequently, the sum of the dilatational term and vortex stretching terms can be written as

$$\omega_i \omega_j S_{ij}^* - \tfrac{2}{3}\theta\omega^2 = \omega^2 \left[\zeta_1 \cos^2(\Lambda_1, \boldsymbol{\omega}) + \zeta_2 \cos^2(\Lambda_2, \boldsymbol{\omega}) + \zeta_3 \cos^2(\Lambda_3, \boldsymbol{\omega}) \right], \quad (4.9)$$

$$\omega_i \omega_j S_{ij}^s = \omega^2 \left[\zeta_1^s \cos^2(\Lambda_1^s, \boldsymbol{\omega}) + \zeta_2^s \cos^2(\Lambda_2^s, \boldsymbol{\omega}) + \zeta_3^s \cos^2(\Lambda_3^s, \boldsymbol{\omega}) \right], \quad (4.10)$$

$$\omega_i \omega_j S_{ij}^{c*} - \tfrac{2}{3}\theta\omega^2 = \omega^2 \left[\zeta_1^c \cos^2(\Lambda_1^c, \boldsymbol{\omega}) + \zeta_2^c \cos^2(\Lambda_2^c, \boldsymbol{\omega}) + \zeta_3^c \cos^2(\Lambda_3^c, \boldsymbol{\omega}) \right]. \quad (4.11)$$

Figure 27 shows the conditional averages of ζ_k and ζ_k^c. In high compression regions, averages of ζ_2 and ζ_3 are all positive and significant, while average ζ_1 is small and negligible. The ratio $\zeta_1 : \zeta_2 : \zeta_3$ is found to be very close to $0:1:1$. Consequently, the overall enstrophy production is enhanced by compression motions and has major contributions from the second and third strain rate eigenvectors rather than the first eigenvector corresponding to the largest compression motion (see figure 28). These
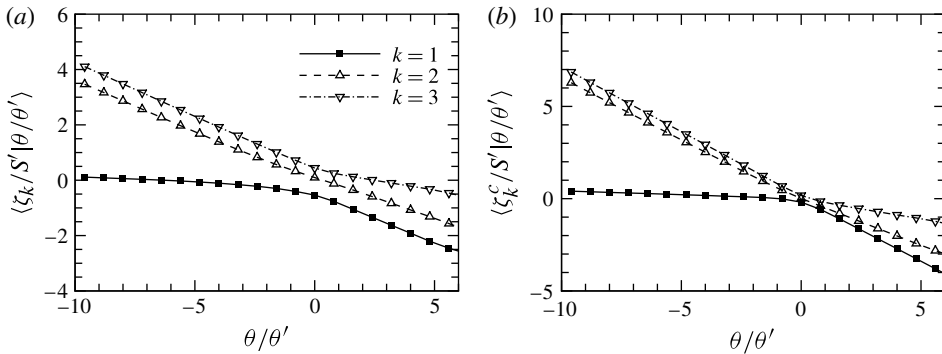
FIGURE 27. Average of ζ_k and ζ_k^c conditioned on the dilatation.
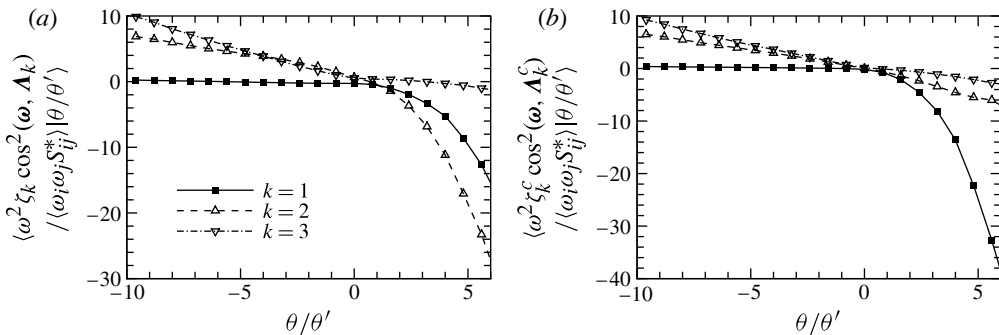
FIGURE 28. Conditional averages of enstrophy production by ζ_k and ζ_k^c.

observations are reasonable since the largest local compression motion along the first eigenvector dominates in compression regions, which gives rise to drastic amplification of perpendicular vorticity components relative to this eigenvector. However, vorticity being strongly compressed along its own direction does not change its magnitude, leading to little effect of local straining on the vorticity component parallel to the first eigenvector in high compression regions.

In high expansion regions, all of the averaged ζ_k become negative, leading to enstrophy destruction by expansion motions (see figure 28). In particular, the largest local expansion motion along the third eigenvector dominates in these regions, indicating the substantial decrease of perpendicular vorticity components relative to this eigenvector. On the other hand, the effect of high expansion motions on the vorticity component parallel to the third strain rate eigenvector is relatively small. Thus, the overall enstrophy destruction has major contributions from the first and second strain rate eigenvectors in high expansion regions (see figure 28).

After Helmholtz decomposition, we observe that the behaviours of ζ_k^c are similar to those of ζ_k, particularly in compression regions. From figure 28, we notice that most of the enstrophy production comes from the compressive velocity component. In expansion regions, enstrophy production $\zeta_2 \cos^2(\boldsymbol{\Lambda}_2, \boldsymbol{\omega})$ from the intermediate eigenvector is larger than $\zeta_1 \cos^2(\boldsymbol{\Lambda}_1, \boldsymbol{\omega})$ from the first eigenvector, due to strong alignment of vorticity with the intermediate eigenvector $\boldsymbol{\Lambda}_2$. Otherwise, for the

θ/θ'	Focal (%)	Non-focal (%)
$[-\infty, +\infty]$	61.7	38.3
$[-\infty, -2.0]$	38.6	61.4
$[-2.0, -1.0]$	52.9	47.1
$[-1.0, -0.0]$	60.5	39.5
$[0.0, 1.0]$	63.6	36.4
$[1.0, 2.0]$	66.5	33.5
$[2.0, +\infty]$	67.8	32.2

TABLE 5. Fractions of the focal and non-focal regions at various dilatation levels.

compressive velocity component, $\zeta_1^c \cos^2(\Lambda_1^c, \boldsymbol{\omega})$ is dominant due to strong alignment of vorticity with the first eigenvector Λ_1^c, in high expansion regions.

5. Effect of compressibility on the local flow topology

We have so far focused on quantifying the effects of local compressibility on volume-averaged statistics and conditional statistics associated with velocity gradients. In this section, we shall instead explore the local flow structures of velocity gradients and how these structures are modified by local compressibility effects. We hope that the structural analysis will complement the statistical results and provide a better understanding of the observed local compressibility effects.

5.1. *Invariants of the velocity gradients*

According to the topological classification of Chong *et al.* (1990), the generalized local flow patterns are fully characterized by three invariants of the velocity gradient tensor $A_{ij} = \partial u_j / \partial x_i$. Let P, Q, R, respectively, denote the first, second and third invariants of A_{ij}, which are defined by

$$P = -(\xi_1 + \xi_2 + \xi_3) = -\theta, \tag{5.1}$$

$$Q = \xi_1\xi_2 + \xi_2\xi_3 + \xi_3\xi_1 = \tfrac{1}{2}\left(P^2 - S_{ij}S_{ij} + \Omega_{ij}\Omega_{ij}\right), \tag{5.2}$$

$$R = -\xi_1\xi_2\xi_3 = \tfrac{1}{3}\left(-P^3 + 3PQ - S_{ij}S_{jk}S_{ki} - 3\Omega_{ij}\Omega_{jk}S_{ki}\right), \tag{5.3}$$

where $S_{ij} = (A_{ij} + A_{ji})/2$, $\Omega_{ij} = (A_{ij} - A_{ji})/2$, respectively, are the strain rate and rotation rate tensors, and ξ_i are the three eigenvalues of the velocity gradient tensor. The discriminant Δ of the velocity gradient tensor is

$$\Delta = 27R^2 + \left(4P^3 - 18PQ\right)R + \left(4Q^3 - P^2Q^2\right). \tag{5.4}$$

The three eigenvalues of A_{ij} are all real if $\Delta < 0$, corresponding to the non-focal regions. On the other hand, in focal regions, $\Delta > 0$; only one eigenvalue is real, and two other eigenvalues are complex conjugate pairs.

Relative fractions of the focal and non-focal regions are shown in table 5. The focal regions fill $\sim 62\%$ of the total volume, very close to the 2/3 obtained by Pirozzoli & Grasso (2004) in a decaying compressible isotropic turbulence with initial turbulent Mach number 0.1–0.8. In addition, we have estimated percentages of the focal and non-focal regions conditioned on the local dilatation. From table 5, we find that compression motion significantly enhances the formation of non-focal structures. On the other hand, expansion motion slightly suppresses the formation of non-focal regions.

θ/θ'	Eddy (%)	Shear (%)	Convergence (%)
$[-\infty, +\infty]$	16.1	45.7	38.2
$[-\infty, -2.0]$	2.5	18.1	79.4
$[-2.0, -1.0]$	8.6	37.8	53.6
$[-1.0, -0.0]$	14.5	45.9	39.6
$[0.0, 1.0]$	17.7	47.4	34.9
$[1.0, 2.0]$	20.6	46.6	32.8
$[2.0, +\infty]$	22.0	45.2	32.8

TABLE 6. Fractions of the eddy, shear and convergence flow structures at various dilatation levels.

Kevlahan, Mahesh & Lee (1992) introduced the deviatoric part of the strain rate tensor $S_{ij}^* = S_{ij} - (S_{kk}\delta_{ij}/3)$ and the antisymmetric velocity gradient (or rotation rate) tensor $\Omega_{ij} \equiv (\partial u_j/\partial x_i - \partial u_i/\partial x_j)/2$ to define three types of flow regions. These are (i) the eddy-dominated region with $\Omega_{ij}\Omega_{ij} > 2S_{ij}^*S_{ij}^*$, (ii) the shear zone with $S_{ij}^*S_{ij}^*/2 \leqslant \Omega_{ij}\Omega_{ij} \leqslant 2S_{ij}^*S_{ij}^*$, and (iii) the convergence zone with $\Omega_{ij}\Omega_{ij} < S_{ij}^*S_{ij}^*/2$.

In table 6, we present the relative fractions of these flow regions conditioned on the local dilatation. Overall, eddy regions, shear zones, and convergence zones occupy $\sim 16, 46$ and 38%, respectively, in rough agreement with the results (21, 44 and 35%) reported by Pirozzoli & Grasso (2004) for a compressible isotropic turbulence. Due to the higher turbulent Mach number in this study, eddy zones are reduced slightly while convergence zones take up slightly more space. When conditioned on dilatation, we find that eddy zones are increased in expansion regions, but are dramatically decreased in compression regions. These tendencies are nearly identical to those of the focal structures since eddy structures occur only in the focal zones as shown in Pirozzoli & Grasso (2004). In contrast, the convergence zones dominate in strong compression regions, but only occupy 33% in expansion regions. Pirozzoli & Grasso (2004) had already reported that convergence regions are essentially non-focal. Thus, compression motions enlarge the percentages of both the non-focal zones and the convergence zones. Shear zones dominate in weak compression and weak expansion regions. The relative fraction of the shear zones is almost independent of the dilatation in expansion regions, but it reduces to only 18% in strong compression regions.

Following Pirozzoli & Grasso (2004), in order to facilitate the discussions of local topological flow structures and clarify the similarities to incompressible turbulence, we introduce the second and third invariants of the deviatoric part of the velocity gradient tensor $(A_{ij}^* = A_{ij} - \theta\delta_{ij}/3)$ as follows:

$$Q^* = \xi_1^*\xi_2^* + \xi_2^*\xi_3^* + \xi_3^*\xi_1^* = -\tfrac{1}{2}\left(S_{ij}^*S_{ij}^* - \Omega_{ij}\Omega_{ij}\right) = Q - \tfrac{1}{3}P^2, \qquad (5.5)$$

$$R^* = -\xi_1^*\xi_2^*\xi_3^* = -\tfrac{1}{3}\left(S_{ij}^*S_{jk}^*S_{ki}^* + 3\Omega_{ij}\Omega_{jk}S_{ki}^*\right) = R - \tfrac{1}{3}PQ + \tfrac{2}{27}P^3, \qquad (5.6)$$

where ξ_i^* are the three eigenvalues of A_{ij}^*. It follows that $\xi_i^* = \xi_i - \theta/3$, where ξ_i are the three eigenvalues of A_{ij}. In addition, ξ_i^* satisfy the following constraint as in the incompressible turbulence:

$$\xi_1^* + \xi_2^* + \xi_3^* = 0. \qquad (5.7)$$

The discriminant of the velocity gradient tensor introduced previously can now be expressed by the new second and third invariants as
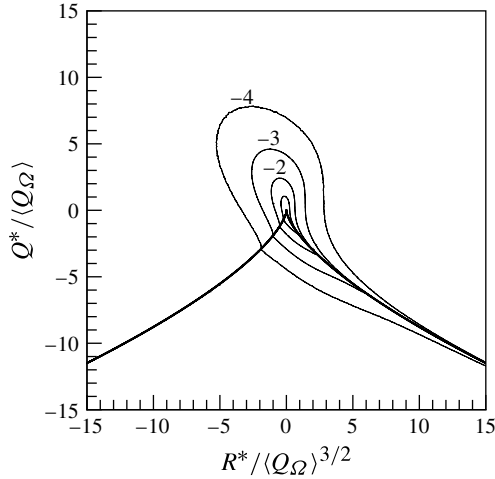
$$\Delta = 27R^{*2} + 4Q^{*3}. \qquad (5.8)$$

FIGURE 29. Isocontour lines of $\log_{10}$ PDF (Q^*, R^*). Four contour lines at $-1, -2, -3, -4$ are shown.

Figure 29 shows the contour lines of the joint p.d.f. of the second and third invariants (Q^*, R^*). The second invariants of the rotation rate tensor $Q_\Omega = \Omega_{ij}\Omega_{ij}/2$ is used to scale the R^* and Q^*, as in the case of incompressible turbulence. Similar to the results by Pirozzoli & Grasso (2004), here we confirm the teardrop shape of the joint p.d.f. of (Q^*, R^*) in compressible turbulence with turbulent Mach number around 1.0. Furthermore, a pronounced longer tail of the joint p.d.f. shape in the fourth quadrant is observed as compared with that in weakly and moderately compressible turbulence (Pirozzoli & Grasso 2004). This behaviour coincides with the enhancement of the convergence zones by the compressibility effect.

Figure 30 displays the contour lines of the joint p.d.f. of (Q^*, R^*) conditioned on the dilatation. The shape of the joint p.d.f. in weak compression and weak expansion regions is almost identical to that in the weakly compressible turbulence (Pirozzoli & Grasso 2004). It is further observed that the statistical preference for points in the second and fourth quadrants is enhanced by the compression motion. In particular, the shape of the joint p.d.f. becomes rather sharp with an extended tail around the right branch of the null-discriminant curve (indicated by the thick solid line) in strong compression regions (figure 30a), leading to the longer tail of the joint p.d.f. of (Q^*, R^*) for the overall flow field when compared with incompressible turbulence. By definition of $Q^* = -(S_{ij}^* S_{ij}^* - \Omega_{ij}\Omega_{ij})/2$, large negative values of Q^* correspond to the regions dominated by the deviatoric strain rate tensor over the rotation rate tensor. Thus, when $\theta/\theta' < -2$, most of the flow volume is occupied by intensive dissipation structures rather than vortex structures. We note that, contrary to our result, a teardrop shape with a normal tail within the shocklets $(\theta/\theta' < -3)$ was reported by Pirozzoli & Grasso (2004). The difference between our results and theirs can be primarily ascribed to the more pronounced compressibility effect in our simulations. In fact, we anticipate that in very high compression regions, many of the eigenvalue ratios $\xi_1:\xi_2:\xi_3$ of the velocity gradient tensor are well approximated by $-1:0:0$. Consequently, we find that $Q^* \approx -P^2/3 \ll 0$, $R^* \approx (2/27)P^3 \gg 0$ and $\Delta = 27R^{*2} + 4Q^{*3} \approx 0$, leading to a long tail of the joint p.d.f. around the right branch of the null-discriminant curve in high compression regions.
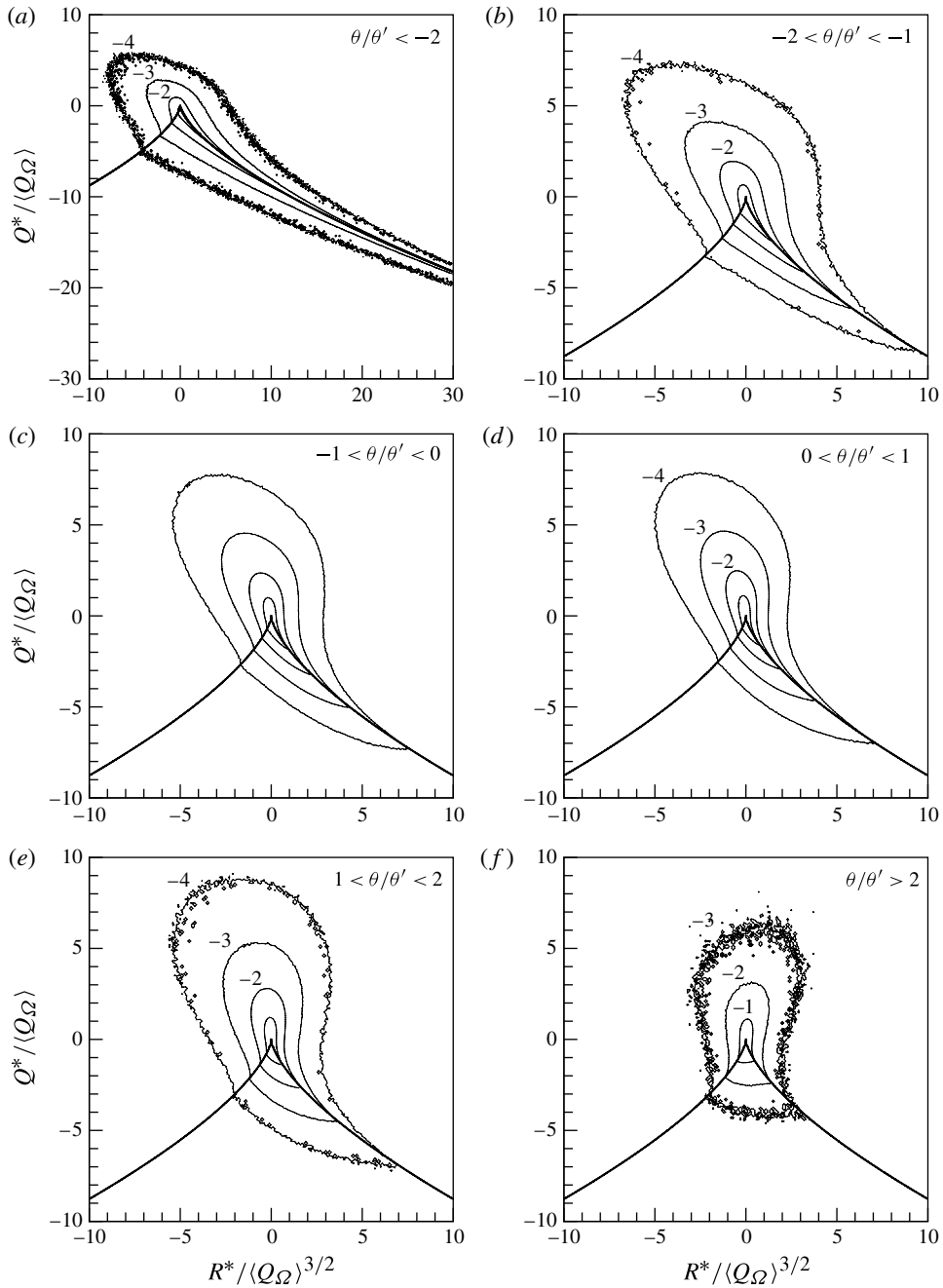
FIGURE 30. Isocontour lines of $\log_{10}$ PDF (Q^*, R^*) at various dilatation levels of θ/θ'. Four contour lines at $-1, -2, -3, -4$ are shown.

On the other hand, the joint p.d.f. becomes more round in shape in expansion regions. Its bottom-right tail is substantially shortened by strong expansion, leading to a nearly symmetric p.d.f. shape with respect to the line $R^* = 0$ when $\theta/\theta' > 2$. The

θ/θ'	$[-\infty, -2.0]$	$[-2.0, -1.0]$	$[-1.0, -0.0]$	$[0.0, 1.0]$	$[1.0, 2.0]$	$[2.0, +\infty]$
Fractions	5.3 %	5.0 %	32.3 %	53.7 %	3.6 %	0.1 %

TABLE 7. Percentage of the enstrophy production $\omega_i\omega_j S_{ij}^*$ in flow regions with various dilatation levels.

substantial noise in the joint p.d.f. for strong expansion regions is due to the lack of sufficient sample points since strong expansion regions occupy only 0.2 % of the total volume.

5.2. *Enstrophy production in various topological structures*

We now examine the enstrophy production by vortex stretching term $\omega_i\omega_j S_{ij}^*$ in various topological structures. Table 7 summarizes percentages of the enstrophy production of the vortex stretching term in flow regions with various dilatation levels. In weakly and moderately compressible regions, the percentage of the vortex stretching enstrophy production is nearly equal to the percentage of the volume occupied by the corresponding value of velocity divergence. In the strong compression regions, however, the percentage of the vortex stretching enstrophy production (5.3 %) is about twice the percentage of the volume (2.5 %) occupied by these regions, due to the enhancement of the vortex stretching by strong compression motion. On the other hand, in the strong expansion regions, the percentage of the vortex stretching term (0.1 %) is about half the percentage of the volume (0.2 %) occupied by these regions, due to the suppression of vortex stretching by strong expansion motions.

The relative contribution of each region in the (Q^*, R^*) plane to the enstrophy production by the vortex stretching term $\omega_i\omega_j S_{ij}^*$ can be expressed as

$$F_{ens}(Q^*, R^*) = \frac{f_{ens}(Q^*, R^*)\, \mathrm{PDF}\,(Q^*, R^*)}{\displaystyle\int_{-\infty}^{\infty}\int_{-\infty}^{\infty} f_{ens}(Q^*, R^*)\, \mathrm{PDF}\,(Q^*, R^*)\, \mathrm{d}Q^*\, \mathrm{d}R^*}, \tag{5.9}$$

and

$$\int_{-\infty}^{\infty}\int_{-\infty}^{\infty} F_{ens}(Q^*, R^*)\, \mathrm{d}Q^*\, \mathrm{d}R^* = 1, \tag{5.10}$$

where $f_{ens}(Q^*, R^*) = \langle \omega_i\omega_j S_{ij}^* \mid Q^*, R^* \rangle$, i.e. the average of vorticity-stretching enstrophy production conditioned on (Q^*, R^*). In figure 31 we plot the contour lines of $F_{ens}(Q^*, R^*)$. A butterfly-like shape of $F_{ens}(Q^*, R^*)$ is observed with a skewed long tail around the right branch of the null-discriminant curve (indicated by the thick solid line). The left part of this $F_{ens}(Q^*, R^*)$ shape is quite similar to the teardrop shape of $\mathrm{PDF}\,(Q^*, R^*)$, and both of them reveal a statistical preference for points in the second and fourth quadrants. These observations reveal that flow structures corresponding to the second and fourth quadrants make substantial contributions to enstrophy production by $\omega_i\omega_j S_{ij}^*$. We note that the left contour levels representing enstrophy production are typically ten times larger than the right contour lines indicating enstrophy destruction. Therefore this figure clearly demonstrates the predominance of vorticity stretching over vorticity compression by the deviatoric strain rate tensor. It also illustrates that the teardrop shape of $\mathrm{PDF}\,(Q^*, R^*)$ is linked to the self-amplification of the vorticity field by the vorticity stretching mechanism.
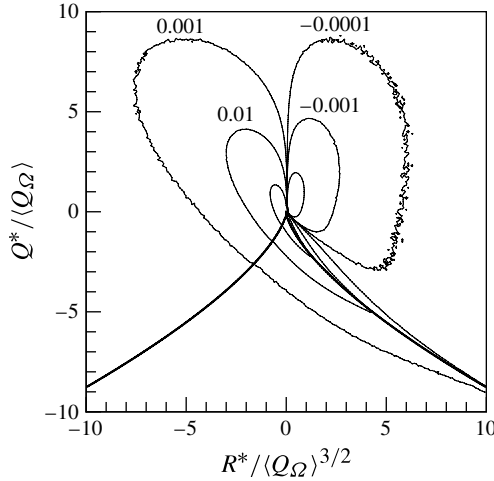
FIGURE 31. Isocontour lines of $F_{ens}(Q^*, R^*)$. Three contour lines of $0.1, 0.01, 0.001$ and three contour lines of $-0.01, -0.001, -0.0001$ are shown.

Figure 32 shows contour lines of $F_{ens}(Q^*, R^*)$ at various dilatation levels. The shape of $F_{ens}(Q^*, R^*)$ is strongly correlated with that of $\mathrm{PDF}(Q^*, R^*)$. We have already observed the enhancement of the statistical preference in the second and fourth quadrants by strong compression motions (see figure 30). Consequently, the enstrophy production $\omega_i\omega_j S_{ij}^*$ is amplified by strong compression motions, consistent with the result for strong compression regions in table 7. In contrast, in strong expansion regions, the symmetric shape of $\mathrm{PDF}(Q^*, R^*)$ gives rise to a tendency of the shape of $F_{ens}(Q^*, R^*)$ to be symmetric. Therefore, the enstrophy destruction by $\omega_i\omega_j S_{ij}^*$ in the first quadrant tends to be of similar magnitude to the enstrophy production by $\omega_i\omega_j S_{ij}^*$ in the second quadrant. Figure 32 helps clarify why the vorticity-stretching enstrophy production $\omega_i\omega_j S_{ij}^*$ is suppressed by strong expansions as shown in table 7.

To include the effect of the dilatational term $-2\theta\omega^2/3$ on enstrophy production, we introduce the distribution function of the overall enstrophy production by $\omega_i\omega_j S_{ij}^* - 2\theta\omega^2/3$ in the (Q^*, R^*) plane as

$$F_{ens}^T(Q^*, R^*) = \frac{f_{ens}^T(Q^*, R^*)\,\mathrm{PDF}(Q^*, R^*)}{\displaystyle\int_{-\infty}^{\infty}\int_{-\infty}^{\infty} f_{ens}^T(Q^*, R^*)\,\mathrm{PDF}(Q^*, R^*)\,\mathrm{d}Q^*\,\mathrm{d}R^*}, \tag{5.11}$$

and

$$\int_{-\infty}^{\infty}\int_{-\infty}^{\infty} F_{ens}^T(Q^*, R^*)\,\mathrm{d}Q^*\,\mathrm{d}R^* = 1, \tag{5.12}$$

where $f_{ens}^T(Q^*, R^*) = \langle \omega_i\omega_j S_{ij}^* - 2\theta\omega^2/3 \,|\, Q^*, R^* \rangle$, i.e. the average of the overall enstrophy production by the stretching term and the dilatational term conditioned on (Q^*, R^*). Figure 33 shows the contour lines of the $F_{ens}^T(Q^*, R^*)$ in the (Q^*, R^*) plane. We find that the contour lines of the $F_{ens}^T(Q^*, R^*)$ are very similar but have slightly broader shapes and longer tails as compared to those in figure 31, implying that the enstrophy-production contribution from the dilatational effect is small relative to that from the vorticity stretching effect in the overall flow field.
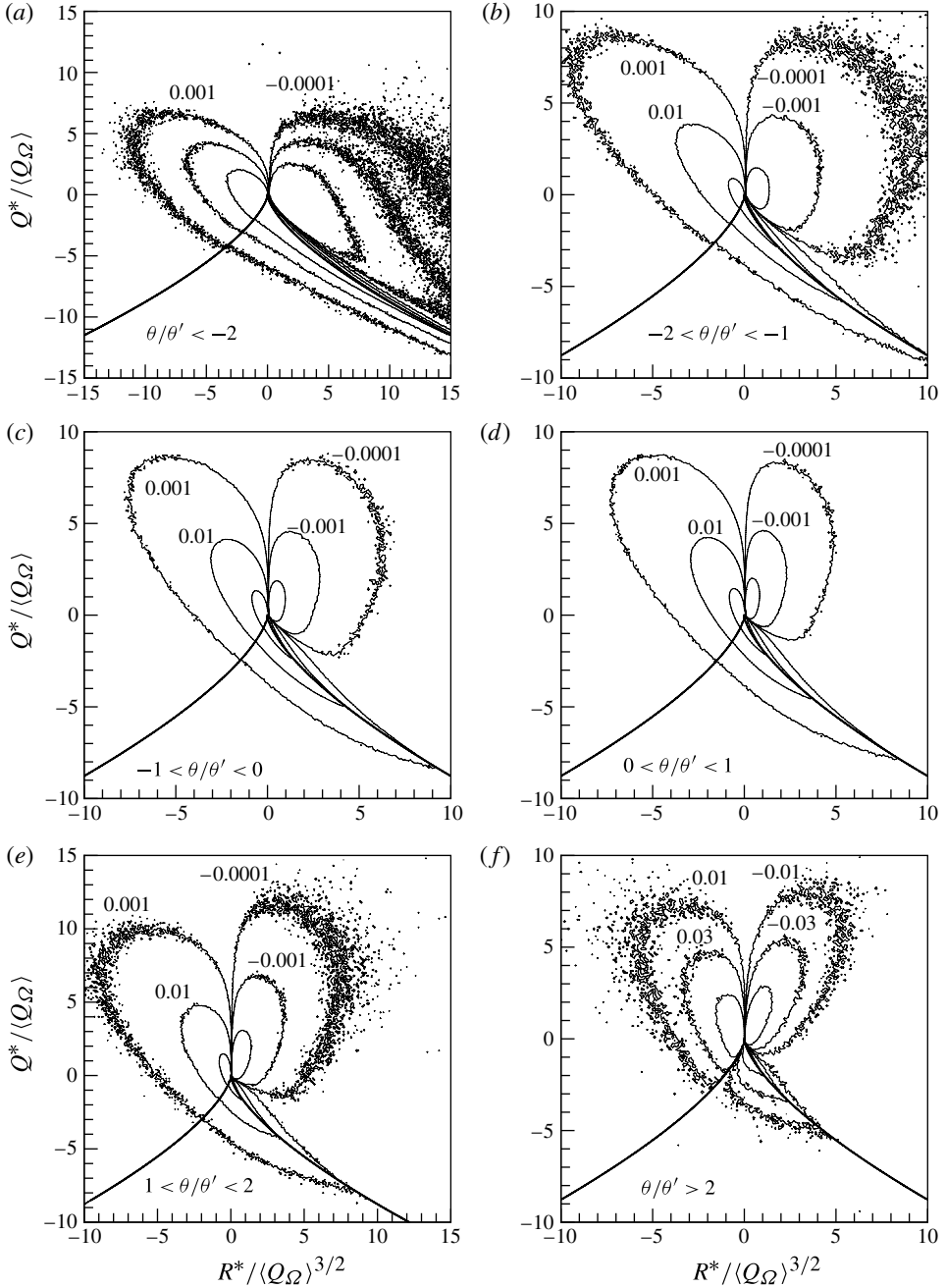
FIGURE 32. Isocontour lines of $F_{ens}(Q^*, R^*)$ at various dilatation levels of θ/θ'. (a) Three contour lines of $0.01, 0.003, 0.001$ and three contour lines of $-0.001, -0.0003, -0.0001$. (b–e) Three contour lines of $0.1, 0.01, 0.001$ and three contour lines of $-0.01, -0.001, -0.0001$. (f) Three contour lines of $0.1, 0.03, 0.01$ and three contour lines of $-0.1, -0.03, -0.01$.
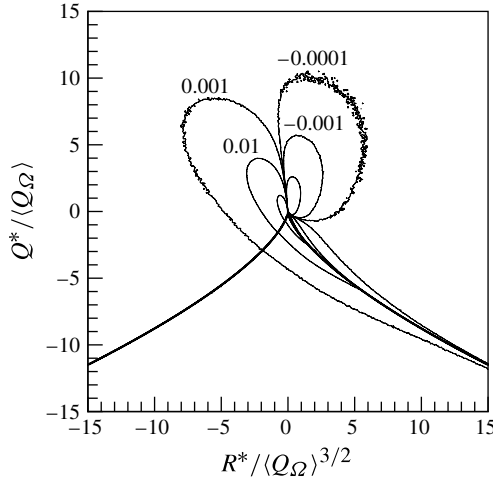
FIGURE 33. Isocontour lines of $F_{ens}^T(Q^*, R^*)$. Three contour lines of 0.1, 0.01, 0.001 and three contour lines of $-0.01, -0.001, -0.0001$ are shown.

Figure 34 shows the contour lines of $F_{ens}^T(Q^*, R^*)$ at various dilatation levels. It is seen that in strong and moderate compression regions, there are no negative levels of the contour lines for $F_{ens}^T(Q^*, R^*)$, implying that the conditional average of enstrophy production is positive in all topological structures in the (Q^*, R^*) plane. In weak compression regions, the negative part of the $F_{ens}^T(Q^*, R^*)$ shape is severely suppressed as compared to the $F_{ens}(Q^*, R^*)$ shape (see figure 32). In contrast, in expansion regions, the positive part of the $F_{ens}^T(Q^*, R^*)$ shape is substantially suppressed as compared to the $F_{ens}(Q^*, R^*)$ shape. In strong expansion regions in particular, all the contour lines for $F_{ens}^T(Q^*, R^*)$ are negative. These observations are consistent with the previous observation that the overall enstrophy production is enhanced by compression motions and suppressed by expansion motions.

5.3. *Invariants of the solenoidal velocity gradients*

We now probe the structures of the solenoidal component of the velocity field. The question here is if the solenoidal component of the velocity field shares similar local topological structures to those of incompressible turbulence. If compressibility has a negligible effect on the solenoidal part of the flow, then we may apply incompressible turbulence models directly to the solenoidal velocity field in highly compressible turbulence, transforming the modelling of compressible turbulence to a somewhat simpler task of modelling only the compressive part of the velocity field.

The solenoidal component of the velocity gradient tensor is denoted by $A_{ij}^s = \partial u_j^s / \partial x_i$. By definition, the three eigenvalues of A_{ij}^s satisfy the incompressibility condition

$$\xi_1^s + \xi_2^s + \xi_3^s = 0. \tag{5.13}$$

The second and third invariants of A_{ij}^s are

$$Q^s = \xi_1^s \xi_2^s + \xi_2^s \xi_3^s + \xi_3^s \xi_1^s = -\tfrac{1}{2} \left(S_{ij}^s S_{ij}^s - \Omega_{ij} \Omega_{ij} \right), \tag{5.14}$$

$$R^s = -\xi_1^s \xi_2^s \xi_3^s = -\tfrac{1}{3} \left(S_{ij}^s S_{jk}^s S_{ki}^s + 3 \Omega_{ij} \Omega_{jk} S_{ki}^s \right), \tag{5.15}$$
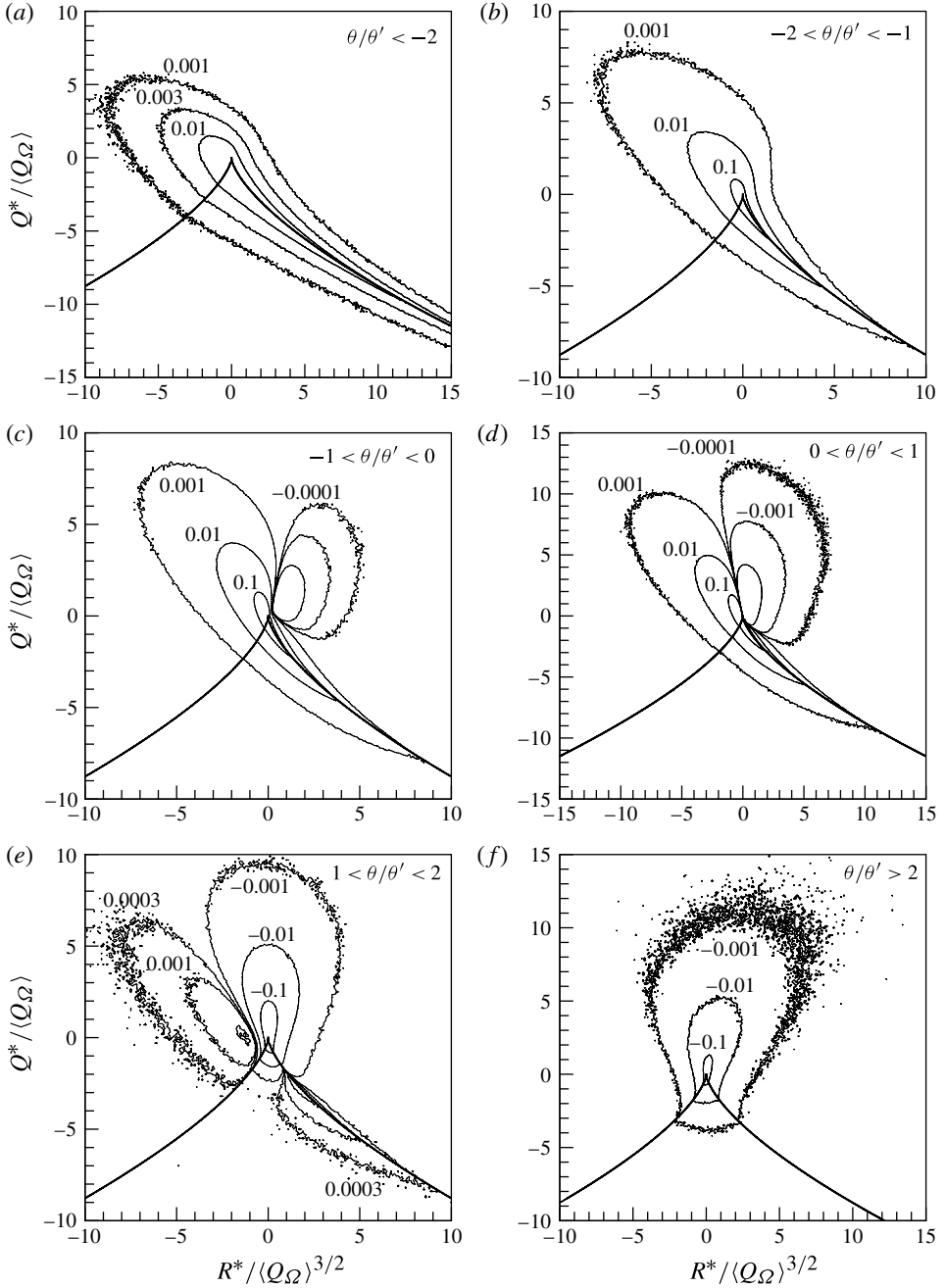
FIGURE 34. Isocontour lines of $F_{ens}^{T}(Q^{*}, R^{*})$ at various dilatation levels of θ/θ'. The levels of contour lines are: (*a*) 0.01, 0.003, 0.001; (*b*) 0.1, 0.01, 0.001; (*c*) 0.1, 0.01, 0.001 and $-0.001, -0.0003, -0.0001$; (*d*) 0.1, 0.01, 0.001 and $-0.01, -0.001, -0.0001$; (*e*) 0.003, 0.001, 0.0003 and $-0.1, -0.01, -0.001$; (*f*) $-0.1, -0.01, -0.001$.

θ/θ'	Focal (%)	Non-focal (%)
$[-\infty, +\infty]$	64.5	35.5
$[-\infty, -2.0]$	67.2	32.8
$[-2.0, -1.0]$	66.7	33.3
$[-1.0, -0.0]$	64.9	35.1
$[0.0, 1.0]$	63.9	36.1
$[1.0, 2.0]$	66.5	33.5
$[2.0, +\infty]$	69.6	30.4

TABLE 8. Fractions of the focal and non-focal regions of the solenoidal velocity field at various dilatation levels.

θ/θ'	Eddy (%)	Shear (%)	Convergence (%)
$[-\infty, +\infty]$	19.7	46.1	34.2
$[-\infty, -2.0]$	22.4	45.2	32.4
$[-2.0, -1.0]$	21.1	46.0	32.9
$[-1.0, -0.0]$	19.7	46.4	33.9
$[0.0, 1.0]$	19.4	46.0	34.6
$[1.0, 2.0]$	21.8	45.0	33.2
$[2.0, +\infty]$	25.1	43.9	31.0

TABLE 9. Fractions of the eddy, shear and convergence flow structures of the solenoidal velocity field at various dilatation levels.

where S_{ij}^s is the solenoidal part of the strain rate tensor. The formulation of the discriminant for A_{ij}^s is identical to that in incompressible turbulence,

$$\Delta^s = 27R^{s2} + 4Q^{s3}. \tag{5.16}$$

In table 8, we present percentages of the volume occupied by focal structures ($\Delta^s > 0$) and non-focal structures ($\Delta^s < 0$) in the solenoidal velocity field. Comparing these data to those shown in table 5, we conclude that the impact of dilatation on these volume fractions is insignificant. A very slight increase of focal region is observed as the dilatation magnitude becomes high. The distribution of focal and non-focal structures is always nearly identical to that in the weakly compressible turbulence (Pirozzoli & Grasso 2004) regardless of the dilatation level.

Table 9 shows the distribution of the flow volume fraction occupied by eddy, shear and convergence structures in the solenoidal part of the velocity field. These data should be compared to the data shown in table 6. Again the dilatation effect is almost negligible. The percentages (20, 46 and 34 %) of the three zones are very close to those (16, 46 and 38 %) found in weakly compressible turbulence (Pirozzoli & Grasso 2004). The dilatation has a weak effect in that it increases slightly the fraction of the eddy zones.

Figure 35 depicts the joint p.d.f. of (Q^s, R^s). The shape of the joint p.d.f. is exactly identical to that of the overall velocity field reported in the weakly compressible flows (Pirozzoli & Grasso 2004). In addition, the joint p.d.f. of (Q^s, R^s) conditioned on the dilatation is shown in figure 36. As indicated by table 9, the p.d.f. shape of (Q^s, R^s) remains nearly unchanged in both strong compression regions and strong expansion
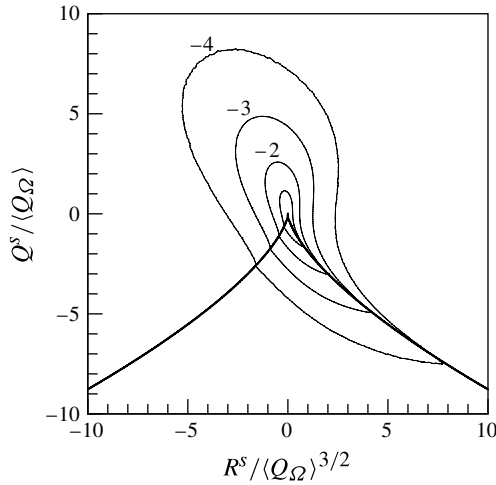
FIGURE 35. Isocontour lines of $\log_{10}$ PDF (Q^s, R^s). Four contour lines of $-1, -2, -3, -4$ are shown.

regions. Therefore, we conclude that the direct effect of local compressibility on the local topology of the solenoidal component of velocity field is indeed negligible.

6. Summary and conclusions

In this paper, a systematic investigation of the statistics and structures of velocity gradients was performed in a simulated, highly compressible turbulence. The turbulent Mach number was 1.03, higher than most previous studies of a similar focus. To evaluate the impact of local fluid compression and expansion, a variety of statistics and geometric structures conditioned on the local dilatation – a measure of local flow compressibility – were analysed. Several important effects of local compressibility were identified, most of which were shown to be associated with the compressive component of the velocity, and some of which significantly impacted the overall flow field.

We discussed the effect of local compressibility on the enstrophy production from a deviatoric strain rate term and a dilatational term using the conditional average. We observed that the overall enstrophy production is enhanced by compression motions and suppressed by expansion motions. In high expansion regions in particular, enstrophy is destroyed very effectively. When enstrophy production was decomposed into a normal component and a tangential component relative to the local density isosurface, we found that the normal component of enstrophy production is negligible in both compression and expansion regions. The effect of the dilatational term is isotropic and makes a major contribution to enstrophy production at high dilatation levels. The enstrophy production from the deviatoric strain rate term is also significant and has much more complex behaviours in various compressible regions. Conditional statistics showed that the enstrophy production from the deviatoric straining, $\omega_i \omega_j S_{ij}^*$, is enhanced by local compression motions and weak expansion motions. However, in strong expansion regions, the net enstrophy production of the deviatoric straining is drastically reduced as the intensity of expansion motions increases. After applied Helmholtz decomposition, it was revealed that the deviatoric straining from the
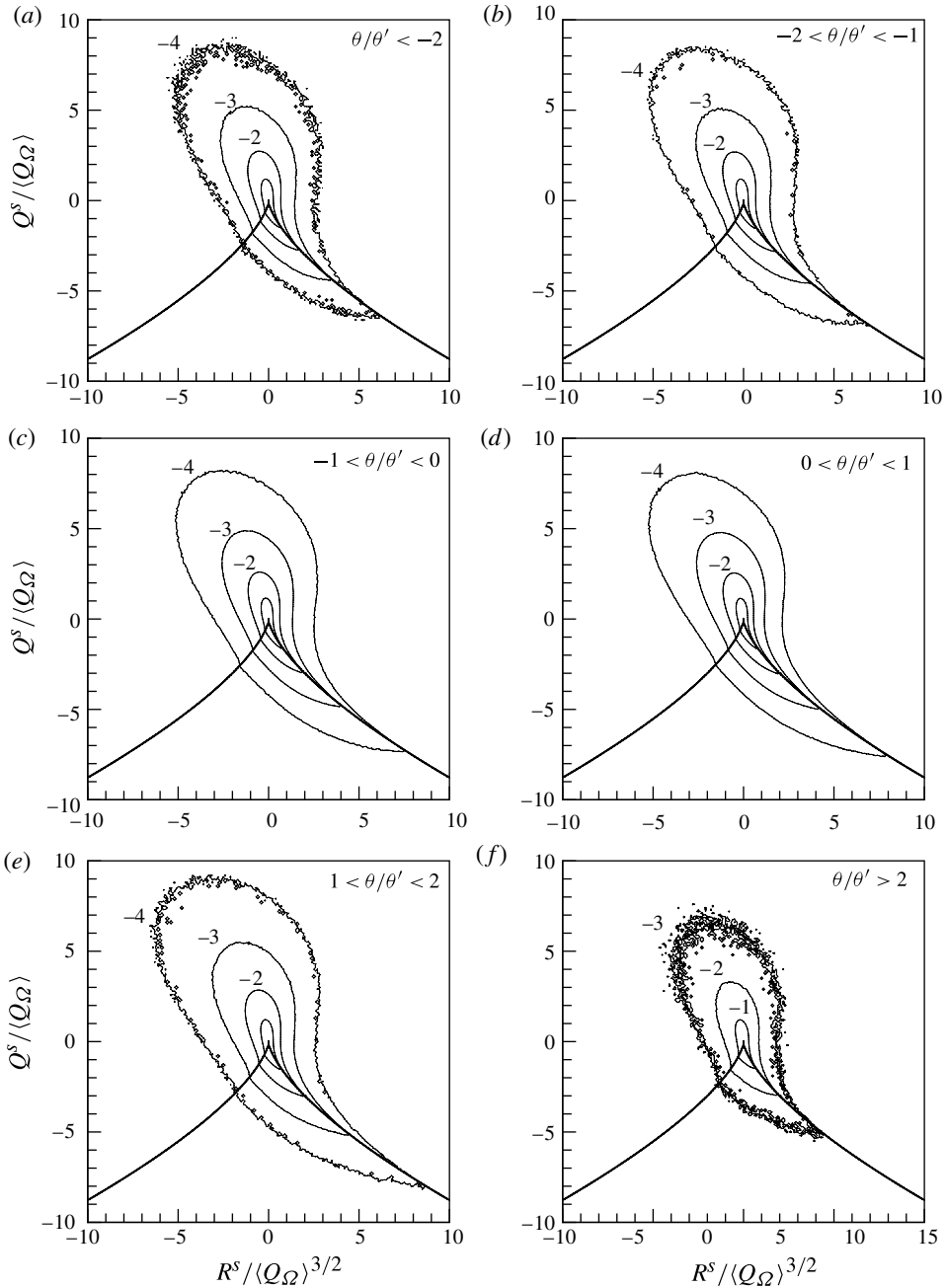
FIGURE 36. Isocontour lines of $\log_{10}$ PDF (Q^s, R^s) at various dilatation levels of θ/θ'. Four contour lines of $-1, -2, -3, -4$ are shown.

solenoidal velocity component always makes a positive contribution to enstrophy production regardless of dilatation levels.

Various properties of the strain rate tensor conditioned on the dilatation were investigated. It was found that in the overall flow field, the most probable eigenvalue

ratio for the strain rate tensor is $-3:1:2.5$, quantitatively different from the preferred eigenvalue ratio of $-4:1:3$ reported in incompressible turbulence (Ashurst *et al.* 1987) and weakly compressible turbulence (Erlebacher & Sarkar 1993; Pirozzoli & Grasso 2004; Lee *et al.* 2009). Furthermore, the strain rate eigenvalue ratio tends to be $-1:0:0$ in high compression regions, implying that sheet-like structures dominate in these regions. It was also shown that in high compression regions, the first strain rate eigenvector (i.e. the one with the most negative eigenvalue) tends to be strongly aligned with the density gradient vector, while in high expansion regions, the third strain rate eigenvector (i.e. the one with the most positive eigenvalue) tends to be aligned with the density gradient vector. These tendencies are more obvious for the strain rate eigenvectors of the compressive velocity component, and for higher dilatation levels.

We further investigated the enstrophy production from the deviatoric straining along three principal directions of the strain rate tensor. The alignment between vorticity and the intermediate eigenvector of the deviatoric strain rate tensor was shown to be almost identical to that in incompressible turbulence. The same alignment was found in expansion regions, but was weakened by strong compression motions. Consequently, we observed that the intermediate strain rate eigenvector makes a significant contribution to the enstrophy production of the deviatoric straining in weakly compressible regions. We also found that, in expansion regions, the vorticity develops a strong tendency to align with the first eigenvector (i.e. the one with the most negative eigenvalue) of the deviatoric strain rate tensor associated with the compressive velocity component, and this tendency becomes stronger as the expansion rate increases. Therefore, the first strain rate eigenvector makes a significant contribution to the enstrophy destruction of the deviatoric straining in high expansion regions. After Helmholtz decomposition, we found that the relative orientations of vorticity with the strain rate eigenvectors of the solenoidal velocity component is insensitive to the change of dilatation levels. We also showed that the enstrophy production from deviatoric straining of the solenoidal velocity component along the intermediate eigenvector is always comparable with that along the third eigenvector.

The effect of local compressibility on local flow structures was analysed using several structure characterization methods. First, the flow topological classification of Chong *et al.* (1990) was employed to partition the flow field into focal and non-focal regions. Second, based on the relative magnitudes of vorticity and deviatoric strain rate, the flow volume was partitioned into eddy, shear, and convergence zones (Kevlahan *et al.* 1992). Third, the joint p.d.f.s of the second and third invariants of the deviatoric velocity gradient tensor, conditioned on the local dilatation, were obtained. We found that compression motions increased the percentages of both non-focal zones and convergence zones. The joint p.d.f. of the second and third invariants exhibited a teardrop shape with a more extended tail in the fourth quadrant, when compared to that for incompressible turbulence. This extended tail was shown to be caused by shock waves in highly compressible turbulence. In contrast, the joint p.d.f. in expansion regions takes a more rounded shape with a shortened bottom-right tail. A nearly symmetric joint p.d.f. was observed in strong expansion regions.

The enstrophy production by vortex stretching term $\omega_i \omega_j S_{ij}^*$ in various topological structures was then quantified. Different structures in the (Q^*, R^*) plane were shown to yield positive and negative vorticity-stretching enstrophy production. The distribution of positive contributions mimics the teardrop shape of the joint p.d.f. of (Q^*, R^*), with both of them having a statistical preference in the second and fourth quadrants. The region of negative contributions lies mostly in the first quadrant of the (Q^*, R^*)

plane, with a magnitude a factor of 10 smaller than that of the positive contribution region. This finding provided a topological demonstration of the predominance of vorticity stretching over vorticity compression. Strong compression enhances the contributions from the second and fourth quadrants, leading to the amplification of the vorticity-stretching enstrophy production. On the other hand, in strong expansion regions, the distribution function is nearly symmetric, and as such the net vorticity-stretching enstrophy generation is significantly suppressed. We also discussed the overall enstrophy production by both the vortex stretching term $\omega_i \omega_j S_{ij}^*$ and the dilatational term $-2\theta \omega^2/3$ in various topological structures. The distribution function was found to be very similar to that of the vortex stretching term for the overall flow field. When conditioned on different levels of velocity divergence, we observed strong tendencies to enhancement of enstrophy production by high compression motions, and again suppression of enstrophy production by high expansion motions.

The universal teardrop shape found in incompressible and weakly compressible turbulent flows was recovered when the invariants were computed using the solenoidal velocity component, which was found to be insensitive to the local dilatation.

The current study, together with our companion papers (Wang *et al.* 2011, 2012), reveals a variety of unique small-scale features in highly compressible turbulence, relative to the usual statistical properties and structures of incompressible turbulence. These new features and departures can be largely understood through the effects associated with the compressive component of the flow. Together we show that the Helmholtz decomposition provides a convenient and logical theoretical framework to model highly compressible turbulence.

REFERENCES

ANDREOPOULOS, Y., AGUI, J. H. & BRIASSULIS, G. 2000 Shock wave–turbulence interactions. *Annu. Rev. Fluid Mech.* **32**, 309–345.

ASHURST, W. T., KERSTEIN, A. R., KERR, R. M. & GIBSON, C. H. 1987 Alignment of vorticity and scalar gradient with strain rate in simulated Navier–Stokes turbulence. *Phys. Fluids* **30**, 2343–2353.

BALSARA, D. S. & SHU, C. W. 2000 Monotonicity preserving weighted essentially non-oscillatory schemes with increasingly high order of accuracy. *J. Comput. Phys.* **160**, 405–452.

BETCHOV, R. 1956 An inequality concerning the production of vorticity in isotropic turbulence. *J. Fluid Mech.* **1**, 497–504.

BLACKBURN, H. M., MANSOUR, N. N. & CANTWELL, B. J. 1996 Topology of fine-scale motions in turbulent channel flow. *J. Fluid Mech.* **310**, 269–292.

CHONG, M. S., PERRY, A. E. & CANTWELL, B. J. 1990 A general classification of three-dimensional flow fields. *Phys. Fluids* A **2**, 765–777.

CHONG, M. S., SORIA, J., PERRY, A. E., CHACIN, J., CANTWELL, B. J. & NA, Y. 1998 Turbulence structures of wall bounded shear flows found using DNS data. *J. Fluid Mech.* **357**, 225–247.

DONZIS, D. A., YEUNG, P. K. & SREENIVASAN, K. R. 2008 Dissipation and enstrophy in isotropic turbulence: resolution effects and scaling in direct numerical simulations. *Phys. Fluids* **20**, 045108.

ERLEBACHER, G. & SARKAR, S. 1993 Statistical analysis of the rate of strain tensor in compressible homogeneous turbulence. *Phys. Fluids* A **5**, 3240–3254.

GALANTI, B. & TSINOBER, A. 2000 A self-amplification of the field of velocity derivatives in quasi-isotropic turbulence. *Phys. Fluids* **12**, 3097–3099.

ISHIHARA, T., KANEDA, Y., YOKOKAWA, M., ITAKURA, K. & UNO, A. 2007 Small-scale statistics in high-resolution direct numerical simulation of turbulence: Reynolds number dependence of one-point velocity gradient statistics. *J. Fluid Mech.* **592**, 335–366.

KEVLAHAN, M., MAHESH, K. & LEE, S. 1992 Evolution of the shock front and turbulence structures in the shock/turbulence interaction. In *Proceedings of the Summer Program 277-292, CTR, Stanford.*

KHOLMYANSKY, M., TSINOBER, A. & YORISH, S. 2001 Velocity derivatives in the atmospheric surface layer at $Re_\lambda = 10^4$. *Phys. Fluids* **13**, 311–314.

LEE, K., GIRIMAJI, S. S. & KERIMO, J. 2009 Effect of compressibility on turbulent velocity gradients and small-scale structure. *J. Turbul.* **10**, 1–18.

LELE, S. K. 1992 Compact finite difference schemes with spectral-like resolution. *J. Comput. Phys.* **103**, 16–42.

LÜTHI, B., TSINOBER, A. & KINZELBACH, W. 2005 Lagrangian measurement of vorticity dynamics in turbulent flow. *J. Fluid Mech.* **528**, 87–118.

MENEVEAU, C. 2011 Lagrangian dynamics and models of the velocity gradient tensor in turbulent flows. *Annu. Rev. Fluid Mech.* **43**, 219–245.

MIURA, H. 2004 Excitations of vortex waves in weakly compressible isotropic turbulence. *J. Turbul.* **5**, 1–22.

MOISY, F. & JIMÉNEZ, J. 2004 Geometry and clustering of intense structures in isotropic turbulence. *J. Fluid Mech.* **513**, 111–133.

OOI, A., MARTIN, J., SORIA, J. & CHONG, M. S. 1999 A study of the evolution and characteristics of the invariants of the velocity-gradient tensor in isotropic turbulence. *J. Fluid Mech.* **381**, 141–174.

PIROZZOLI, S. & GRASSO, F. 2004 Direct numerical simulations of isotropic compressible turbulence: influence of compressibility on dynamics and structures. *Phys. Fluids* **16**, 4386–4407.

PORTER, D., POUQUET, A. & WOODWARD, P. 2002 Measures of intermittency in driven supersonic flows. *Phys. Rev.* E **66**, 026301.

SAMTANEY, R., PULLIN, D. I. & KOSOVIC, B. 2001 Direct numerical simulation of decaying compressible turbulence and shocklet statistics. *Phys. Fluids* **13**, 1415–1430.

DA SILVA, C. B. & PEREIRA, J. C. F. 2008 Invariants of the velocity-gradient, rate-of-strain, and rate-of-rotation tensors across the turbulent/nonturbulent interface in jets. *Phys. Fluids* **20**, 055101.

SORIA, J., SONDERGAARD, R., CANTWELL, B. J., CHONG, M. S. & PERRY, A. E. 1994 A study of the fine-scale motions of incompressible time-developing mixing layers. *Phys. Fluids* **6**, 871–884.

SUMAN, S. & GIRIMAJI, S. S. 2010 Velocity gradient invariants and local flow field topology in compressible turbulence. *J. Turbul.* **11**, 1–24.

TSINOBER, A., KIT, E. & DRACOS, T. 1992 Experimental investigation of the field of velocity gradients in turbulent flows. *J. Fluid Mech.* **242**, 169–192.

WANG, L.-P., CHEN, S., BRASSEUR, J. G. & WYNGAARD, J. C. 1996 Examination of hypotheses in the Kolmogorov refined turbulence theory through high-resolution simulations. Part 1. Velocity field. *J. Fluid Mech.* **309**, 113–156.

WANG, J., SHI, Y., WANG, L.-P., XIAO, Z., HE, X. T. & CHEN, S. 2011 Effect of shocklets on the velocity gradients in highly compressible isotropic turbulence. *Phys. Fluids* **23**, 125103.

WANG, J., SHI, Y., WANG, L.-P., XIAO, Z., HE, X. T. & CHEN, S. 2012 Scaling and statistics in three-dimensional compressible turbulence. *Phys. Rev. Lett.* **108**, 214505.

WANG, J., WANG, L.-P., XIAO, Z., SHI, Y. & CHEN, S. 2010 A hybrid numerical simulation of isotropic compressible turbulence. *J. Comput. Phys.* **229**, 5257–5279.